INORGANIC CHEMISTRY FRONTIERS

RESEARCH ARTICLE

View Article Online
View Journal

Cite this: DOI: 10.1039/d5qi02205c

Photocatalytic arylterpyridine iridium(III) complexes trigger oncosis in 2D and 3D cancer cell models *via* NADH oxidation

Isabel Romero-Castellón, †[a] Lenka Markova, †[b] María José Piernas-Muñoz, [a] Hana Kostrhunova, [b,c] Jana Kasparkova, [c] Christoph Janiak, [d] Marta E. Alberto, [e] Antonio Francés-Monerris, *[f] José Ruiz *[a] and Viktor Brabec *[c]

Eight novel arylterpyridine iridium(III) complexes [Ir(N^N^N)(C^N)Cl]PF_6 (**Ir1–Ir8**), incorporating diverse *para*-substituents and extended aromatic groups, were synthesized and fully characterized. Upon exposure to biocompatible blue light, all complexes demonstrated potent antiproliferative effects in both 2D and 3D cancer cell models, with minimal toxicity toward non-cancerous cells. Complexes **Ir2**, **Ir3**, and **Ir8** – those containing 9-anthracenyl-, 1,3-benzodioxole-5-yl, and 1,4-benzodioxan-6-yl substituents, respectively – exhibited the highest phototoxic indices and were further investigated. **Ir2** and **Ir3** preferentially localized in the cytoplasm of HCT116 cells, inducing oncotic-like cell death upon irradiation, characterized by distinct cellular morphological changes, adenosine triphosphate (ATP) depletion, and porimin upregulation. Mechanistic studies revealed that photoactivated **Ir2** and **Ir3** catalyzed nicotinamide adenine dinucleotide (NADH) oxidation with high turnover frequencies, accompanied by the generation of reactive oxygen species (ROS). Molecular dynamics and hybrid QM/MM simulations supported the formation of non-covalent Ir–NADH heterodimers, with Mulliken charge analysis indicating NADH → Ir charge transfer stabilized triplet states and identifying **Ir8** as the most efficient NADH photocatalyst, in agreement with the experimental evidence obtained by intracellular NAD^+/NADH assays. Collectively, these findings establish a mechanistic framework for a novel class of photoactivated iridium complexes that exert synergistic phototoxic and photocatalytic effects, offering a promising alternative to conventional ROS-driven photodynamic therapy.

Received 30th October 2025,
Accepted 23rd December 2025

DOI: 10.1039/d5qi02205c

rsc.li/frontiers-inorganic

Introduction

Photodynamic therapy (PDT) is a clinically approved form of cancer treatment (*e.g.*, bladder, lung, brain, and esophageal cancers) as well as used for treatment of bacterial, viral, and fungal infections which enables localized drug activation using a photosensitizer (PS), light, and molecular oxygen.[1] This targeted mechanism reduces systemic toxicity and side effects compared to chemotherapy.[2,3] PSs further enhance spatiotemporal precision, and PDT may also stimulate antitumor immune responses.[4–7] Under light exposure, PSs are excited from the ground state (S_0) to an excited state (S_x), which then reaches the triplet excited state (T_1) through intersystem crossing (ISC). Subsequently, the excess energy from light absorption by the photosensitizer can either be transferred to molecular oxygen to generate singlet oxygen (type II PDT) or interact with surrounding biomolecules *via* electron or hydrogen transfer to produce reactive oxygen species (ROS) such as superoxide or hydroxyl radicals (type I PDT).[8] Among the two main mechanisms of PDT, the type II mechanism, which relies on the generation of singlet oxygen ($^1O_2$), is inherently limited by its dependence on molecular oxygen as a co-reactant. Conversely, the photogeneration of type I reactive oxygen species (ROS) enhances the efficacy of PDT under

[a]*Departamento de Química Inorgánica, Universidad de Murcia, and Murcia BioHealth Research Institute (IMIB-Arrixaca), E-30100 Murcia, Spain. E-mail: jruiz@um.es*
[b]*Institute of Biophysics, Czech Academy of Sciences, Kralovopolska 135, CZ-61200 Brno, Czech Republic*
[c]*Department of Biophysics, Faculty of Science, Palacky University, Slechtitelu 27, CZ-78371 Olomouc, Czech Republic. E-mail: vbrabec44@gmail.com*
[d]*Institut für Anorganische Chemie und Strukturchemie, Heinrich-Heine-Universität Düsseldorf, Universitätsstrasse 1, D-40225 Düsseldorf, Germany*
[e]*Dipartimento di Chimica e Tecnologie Chimiche, Università della Calabria, Arcavacata di Rende I-87036, Italy*
[f]*Institut de Ciència Molecular, Universitat de València, P.O. Box 22085, València 46071, Spain. E-mail: antonio.frances@uv.es*
† These authors contributed equally to this work.

hypoxic conditions.[9] Recently, transition metal complexes (TMCs) have emerged as promising systems for anticancer PDT,[10] with Ru(II)- and Ir(III)-based PSs advancing to early-stage preclinical and clinical applications.[11–17] Among these, Ru(II) polypyridyl complexes show significant potential to overcome some of the limitations of current PSs.[18–21] An outstanding example is TLD-1433, currently in phase II clinical trials for the intravesical treatment of non-muscle-invasive bladder cancer (NMIBC), which is activated by green light (NCT03945162).[22] In recent years, Ir(III) complexes have also garnered significant attention due to their favorable chemical and photophysical properties, including high chemical stability, photostability, strong emission, and efficient light-activated ROS generation.[23–26]

A well-known example of a tridentate N^N^N-type ligand is 2,2′:6′,2″-terpyridine (tpy), shown in Fig. S1A, which features three nitrogen donor atoms from its heteroaromatic rings and exhibits strong affinity for metal cations. Iridium terpyridine complexes have demonstrated remarkable adaptability in medicinal chemistry, serving as versatile molecular building blocks in photocatalysis and phototherapy.[27] The introduction of tridentate ligands can suppress chirality, thereby preventing the formation of stereoisomers and reducing the risk of undesirable side effects.[28] At the same time, nicotinamide adenine dinucleotide (NADH) is crucial for redox balance and metabolism, and its elevated demand in cancer cells makes it a strategic target for anticancer phototherapy.[29–31] Sadler *et al.* first introduced the concept of photocatalytic therapy (PCT), reporting the in-cell photo-oxidation of NADH by the iridium complex [Ir(CH_3-Phtpy)(pq)Cl]PF_6, containing a *p*-tolyl-substituted terpyridine (CH_3-Phtpy) ligand and cyclometalated 3-phenylisoquinoline (pq) as a co-ligand (Fig. S1B),[32] which initiated tandem intracellular photocatalysis, disrupted the mitochondrial ETC (electron transport chain), and depleted ATP (adenosine triphosphate) in cancer cells. Following this research, Huang and Banerjee *et al.* reported a novel dinuclear Ir(III) photocatalyst for cancer therapy, revealing the synergistic effect of the additional Ir(III) center and ruling out an additive effect (Fig. S1C).[33] Chao *et al.* have recently reported the induction of immunogenic cell death in melanoma stem cells by photo-activation of a ferrocene–iridium(III) prodrug (Fig. S1D).[34] Brabec *et al.* have also demonstrated that the cyclometalated Ir(III) complex shown in Fig. S1E holds promise for the targeted therapy of resistant brain tumors when photo-activated.[35] On the other hand, a bis-tridentate Ir(III) complex (Fig. S1F) has exhibited potential as an effective antibacterial agent *via* a synergistic photocatalytic and photodynamic mechanism of action.[36]

Extending π-conjugation is a well-established strategy to enhance the electronic properties of ligands and enable applications in fields such as catalysis, anticancer drug development for PDT, and antimicrobial photodynamic therapy (aPDT).[37] In the present work, we explored a series of eight new substituted terpyridine iridium(III) complexes, **Ir1–Ir8** (Scheme 1), each of which incorporates an aromatic group at the 4′-position of the central pyridine ring of the tpy scaffold. To exploit their expanded π-conjugation and rigid planar structures, which are known to enhance photosensitivity and stabilize excited states,[38] 1-naphthyl and 9-anthracenyl groups were employed. In addition, 4′-phenylterpyridine derivatives bearing –Cl, $–CF_3$, $–CO_2Me$, and 9*H*-carbazol-9-yl at the *p*-position, as well as 1,3-benzodioxole-5-yl or 1,4-benzodioxan-6-yl substituents were selected as ligands. It is well known that –Cl, $–CF_3$, and $–CO_2Me$ are electron-withdrawing groups. In contrast, the carbazole moiety—an aromatic heterocycle containing nitrogen—is distinguished by its strong electron-donating properties.[39] For its part, the electron-rich aromatic framework and conjugated system of 1,3-benzodioxole derivatives have been associated with notable bioactivity, making them promising scaffolds for the design of small molecules.[40]

Herein, we focused on the characterization and biological evaluation of a new class of substituted terpyridine iridium(III)

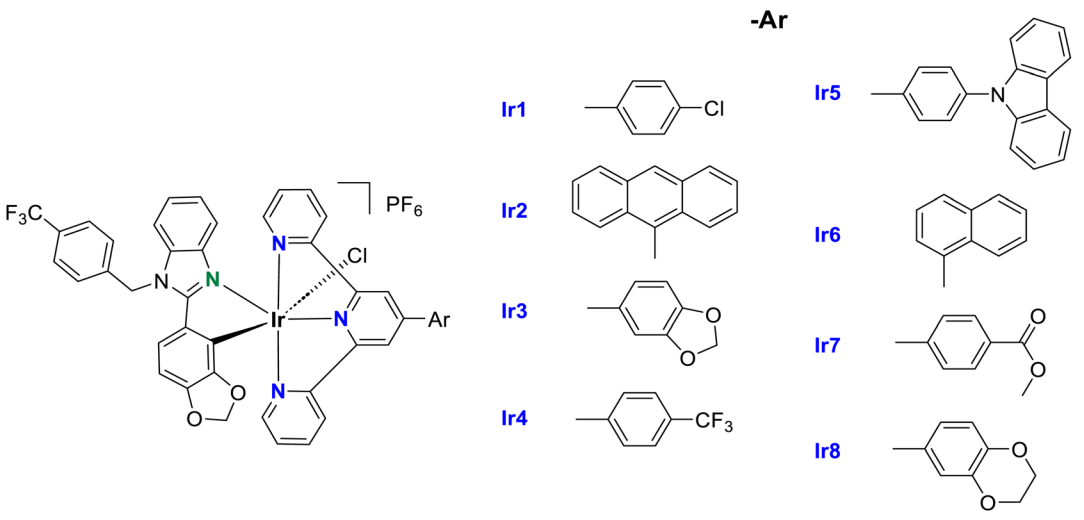

Scheme 1 General structures of the new arylterpyridine Ir(III) complexes synthesized in this work.

complexes, **Ir1–Ir8**. This study pays special attention to determining the ability of these compounds to act as photoredox catalysts and to elucidating the mechanism underlying their antiproliferative activity in cancer cells, specifically focusing on in-cell NADH photocatalysis as a strategy to overcome the limitations of hypoxia and drug resistance in conventional therapies.[41]

Results and discussion

Design, synthesis, and chemical characterization of ligands and novel Ir(III) complexes

Ligand **L1** was acquired commercially. Arylterpyridine (Ar-tpy) ligands **L2–L8** (Fig. S2) were prepared *via* condensation between 2-acetylpyridine and the corresponding aldehyde (Scheme S1), following the procedure described by Hanan *et al.*[42] However, ligand **L7** was obtained through a two-step synthetic procedure, involving the methodology outlined above, followed by a subsequent Fischer esterification.[43] On the other hand, the cyclometalating proligand **HC^N** was synthesized in a two-step reaction (Scheme S2). First, upon condensation between 1,3-benzodioxole-5-carboxaldehyde and 1,2-phenylenediamine, the intermediate 2-(benzo[*d*][1,3]dioxol-5-yl)-1*H*-benzo[*d*]imidazole was afforded. Then, this intermediate was reacted with 4-(trifluoromethyl)benzyl bromide to yield the proligand 2-(1,3-benzodioxol-5-yl)-1-(4-(trifluoromethyl) benzyl)-1*H*-benzo[*d*]imidazole.

The precursor complexes [Ir(N^N^N)Cl_3], **A1–A8** (Scheme S3), were synthesized according to the method described by Berndhard *et al.*[44] and Ruiz *et al.*[43] Briefly, $IrCl_3{\cdot}3H_2O$ and ligands **L1–L8** were left to react stoichiometrically. Subsequently, the corresponding monomeric Ir(III) precursor, the cyclometalating proligand **HC^N** and potassium hexafluorophosphate were dissolved in ethylene glycol and subjected to microwave irradiation at 230 °C for 15 min to yield the new iridium complexes [Ir(N^N^N)(C^N)Cl]PF_6, **Ir1–Ir8** (Scheme 1).

The new Ir(III) complexes were then thoroughly characterized by ^{1}H, ^{13}C, and ^{19}F NMR spectroscopy (Fig. S3–S26) and high-resolution electron spray ionization mass spectrometry (HR-ESI-MS). In the ^{1}H NMR spectra of complexes **Ir1–Ir8**, the protons on the central pyridine ring of the arylterpyridine ligand appear as a characteristic singlet (2H) at approximately 9.2 ppm.[43] The –OCH_2O– group resonance associated with the C^N ligand of the new complexes can be distinguished as a singlet at approximately 5.3–5.4 ppm, except for complexes **Ir2** and **Ir6**, whose signal appears at around 5.6–5.7 ppm, due to the presence of additional aromatic rings. Particularly, the **Ir3** complex exhibits a singlet at 6.2 ppm, attributed to the –CH_2– group of the 1,3-benzodioxole moiety associated with the terpyridine ligand. The equivalent –CH_2– of the 1,4-benzodioxan-6-yl scaffold in complex **Ir8** is detected, however, at 4.39 ppm. For its part, the **Ir7** complex exhibits a singlet at *ca.* 3.95 ppm, assigned to –Me in the –COOMe group of the N^N^N ligand. Furthermore, the ^{19}F NMR spectra of all complexes show a singlet near −60.9 ppm, corresponding to the –CF_3 group of the C^N ligand and a doublet at −70 ppm, associated with the PF_6^- anion. Additionally, in the ^{19}F NMR spectrum of complex **Ir4**, an extra singlet can be identified, attributed to the –CF_3 group of the arylterpyridine ligand **L4**. The correlation between these signals and the cleanliness of the spectra, where no significant impurities are observed, serves as evidence of the complexes' purity. The ESI-MS spectra, carried out in positive-ion mode, displayed the corresponding $[M - PF_6]^+$ peaks along with the expected isotopic distribution pattern (Fig. S27–S34). The purity of the complexes was further validated by elemental analysis of C, H and N as well as by reverse-phase high-performance liquid chromatography-mass spectrometry (RP-HPLC-MS) (Fig. S35–S43). All chromatograms display a single peak, achieving a purity percentage higher than 95% in each case (Fig. S35). Complex **Ir5** appears to be the most lipophilic compound in the series and exhibits the lowest accumulation. The latter is probably due to aggregation phenomena associated with the presence of the carbazole moiety in the terpyridine ligand, since carbazole units exhibit a strong tendency to π–π stacking, which may promote self-aggregation in aqueous or biological environments. Such aggregation can hinder the membrane permeability or intracellular diffusion, ultimately limiting effective intracellular uptake.[45]

Crystal structure by X-ray diffraction

Orange crystals of complex **Ir3**·0.5CH_2Cl_2 suitable for X-ray diffraction analysis were obtained through the slow evaporation of hexane into a saturated dichloromethane solution of **Ir3** at room temperature. Crystallographic data and selected metrical parameters for **Ir3** are given in Tables S1 and S2, respectively. A perspective view of the **Ir3** complex is shown in Fig. S44. The iridium(III) center adopted a distorted octahedral coordination geometry with the N3/N4/N5 atoms of the Ar-tpy ligand, the N1/C9 atoms of the C^N ligand, and a monodentate chloride ligand. The N3/N4/N5 atoms are in a meridional arrangement. The chloride ligand is in a *trans* position to the C9 atom, and the Ir–Cl bond length (2.4518(9) Å) is much longer than those of other coordination bonds, as previously reported for iridium analogs.[32] A PF_6 anion balances the monocationic charge of the complex. There are additional disordered CH_2Cl_2 solvent molecules in the crystal structure (Fig. S45) from the crystallization process. The crystal structure is stabilized by both inter- and intramolecular interactions (see Schemes S4 and S5, Tables S3–S5, and Fig. S46 and S47 in the SI for a more detailed discussion and illustrations). Supramolecular packing interactions were analyzed using PLATON. The π–π interactions between the N^N^N ligands of **Ir3** are depicted in Fig. S46a, with the shortest distance between centroids for **Ir3** of 3.727 Å. C–H···π interactions are illustrated in Fig. S46b, while C–H···F interactions are shown in Fig. S47.

Optical properties

Absorption properties and time-dependent density functional theory (TD-DFT) calculations. The absorption spectra of

Ir1–Ir8 (10 μM) were recorded in aerated acetonitrile and water (containing 1% DMSO (dimethyl sulfoxide) in the latter), showing broad absorption bands across the UV/Vis region (Fig. 1A and S48, Table S6). All the cyclometalated iridium(III) complexes exhibit intense absorption bands below 340 nm, which can be attributed to ligand-centered (IL) π–π* electronic transitions localized on the C^N ligand, with some MLCT/LLCT (metal to ligand charge transfer/ligand to ligand charge transfer) mixing character in some transitions, as confirmed by TD-DFT predictions for compounds **Ir2**, **Ir3**, and **Ir8**.[46–50] Natural transition orbitals,[51] which elucidate the nature of the excited state only with one or two couples of orbitals, are shown in Fig. S49–S51, whereas the band assignations are listed in Table S7.

As observed in Fig. 1A and Table S6, the **Ir2** complex, which incorporates a 9-anthracenyl group in the tridentate scaffold, exhibits an enhanced absorption intensity around 250 nm—showing the highest molar extinction coefficient in the series—due to the additional conjugation existing in the moiety. Importantly, all complexes exhibit less intense, lower-energy absorption bands between 350 and 450 nm, with experimental maxima recorded between 380 and 400 nm for all complexes (see Table S6).

The TD-DFT obtained spectra are consistent with the experimental data, with a broad band in that spectral region arising from several low-intensity electronic excitations. Notably, the choice of the Ar substituent gives rise to distinctive and intriguing features. In the case of **Ir2**, the $^1B_{2u}$ π,π* transition at 378 nm (S_9 state), localized on the anthracene ligand (labeled as IL_{Ar}, see Fig. S49 and Table S7), is mainly responsible for the experimental absorption feature, also in agreement with experimental measurements for anthracene dissolved in acetonitrile[52,53] and previous theoretical predictions.[54,55] Such a peculiar IL state localized on the Ar substituent disappears when the ligand is changed. Indeed, three main transitions with mixed ligand-to-ligand charge transfer (^{1}LLCT) and metal-to-ligand charge transfer (^{1}MLCT) nature computed at 426 (S_3), 422 (S_4), and 406 (S_5) nm (Fig. S50 and Table S7) contribute to the broad band in this region found for **Ir3**. Analogously, transitions of the same mixed nature (^{1}MLCT/^{1}LLCT) at 402 and 416 nm were detected in the computed spectrum of **Ir8** (Fig. S51 and Table S7).

Notably, weaker shoulder bands are also observed in the 450–550 nm range (blue-green region) for all species which are associated with dark ^{1}LLCT and spin-forbidden ^{3}MLCT states, due to the spin–orbital coupling of the heavy Ir(III) atom (ζ = 3909 cm^{-1}).[56,57] TD-DFT computations support this ascription. All complexes exhibit an S_1 state with ^{1}LLCT character in their singlet–singlet spectra, yet distinct differences can still be observed. A clear charge transfer from anthracene toward the tpy ligand characterizes the S_1 state of **Ir2** computed at 496 nm ($^1LLCT_{Ar\rightarrow tpy}$), in line with the peculiar anthracene-based HOMO and tpy-based LUMO orbitals found for **Ir2** (see Fig. S52). In contrast, the different nature of HOMO orbitals for **Ir3** and **Ir8**, now mainly localized on the C^N ligand, leads to S_1 states with dominant $^1LLCT_{N^C\rightarrow tpy}$ character mixed with $MLCT_{Ir\rightarrow tpy}$, computed at 478 and 477 nm, respectively.

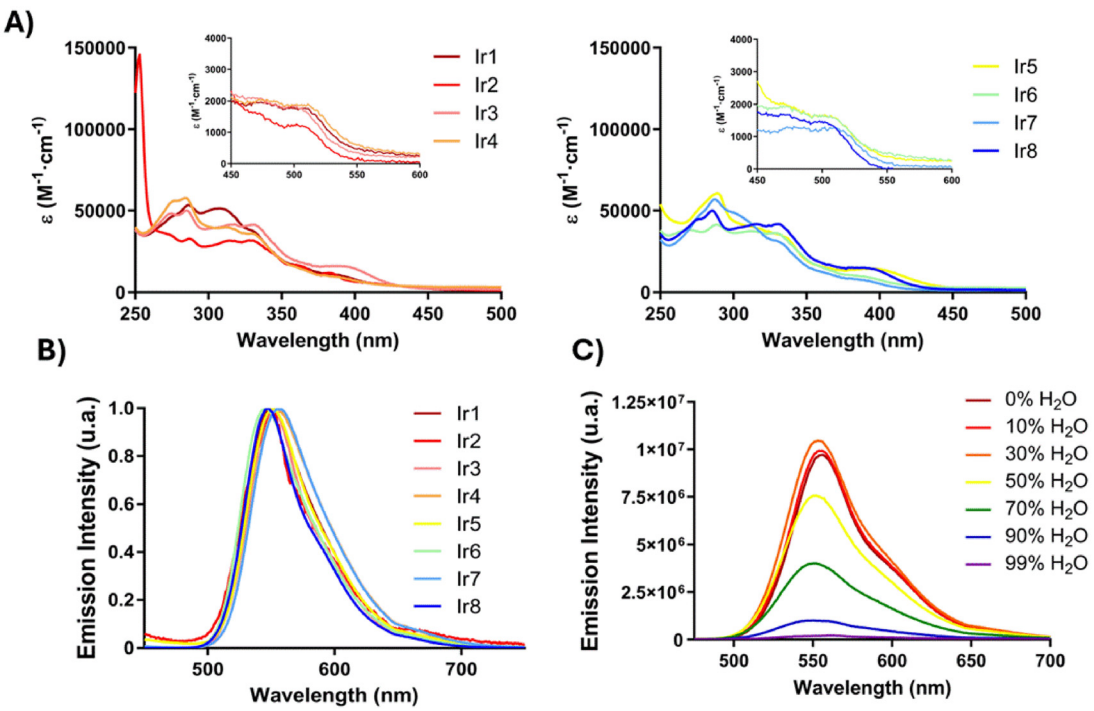

Fig. 1 (A) UV/Vis spectra of **Ir1–Ir8** (10 μM) in aerated acetonitrile. (B) Normalized emission spectra of **Ir1–Ir8** (10 μM) in aerated acetonitrile. (C) Emission spectra of **Ir3** in different DMSO : H_2O mixtures.

The lowest-energy triplet state (T_1) for **Ir3** and **Ir8** is of dominant ^{3}MLCT nature and is predicted at λ = 493 and 491 nm, respectively (Fig. S53). On the other hand, the T_1 and T_2 states of **Ir2** are both localized over the anthracene moiety, whereas the optically active first ^{3}MLCT state (T_3) is vertically predicted at λ = 494 nm, consistent with the slight absorption registered in this area shown in Fig. 1A. The involvement of the heavy Ir atom in ^{3}MLCT leads to large singlet–triplet spin–orbit couplings (SOCs), thereby enabling fast and effective intersystem crossing (ISC) that allows triplet-state population by direct light absorption.[58] SOC values are listed in Table S8, whereas Fig. S54 simulates the absorption spectra of **Ir2**, **Ir3**, and **Ir8**, including SOC, demonstrating the absorption capacities of the complexes in the 450–550 nm region. The triplet nature of these excited states renders them suitable for PDT.[59]

Emission properties and TD-DFT calculations. All new Ir(III) complexes show an emission band in aerated acetonitrile, showing only minor variations in their maximum λ_{em} (540–552 nm, in the green region), regardless of the arylterpyridine N^N^N ligand present on it (Fig. 1B and S55, Table S9). This finding suggests that the emissive state is localized over a molecular moiety common to all complexes, such as the Ir atom and its nearby coordination sphere. Fig. S53 shows that the T_1 state of **Ir3** and **Ir8** is of dominant ^{3}MLCT nature, with partial ^{3}LLCT mixing for the former complex, while both the T_1 and T_2 states of **Ir2** are localized over the anthracene moiety. The spectral shapes reported in Fig. 1B and the relatively low singlet–triplet SOCs calculated for the T_1 state of **Ir2** (Table S8), accordingly with its mainly organic character, suggest that this state is only marginally populated in the excited-state dynamics of this complex and that the emissive state is the lowest-energy ^{3}MLCT state (T_3 state, Fig. S53).

The emission lifetimes (τ_{em}) and quantum yields (ϕ_{em}) of complexes **Ir1–Ir8** were recorded in deaerated acetonitrile at room temperature (see Table S9). Lifetime values vary significantly, ranging from 230 ns (**Ir2**) to 1.08 μs (**Ir8**), and are attributed to a prevailing ^{3}MLCT state, as mentioned above.[60] The emission intensity in deaerated acetonitrile varies notably depending on the structure of the terpyridine ligand, with the 9-anthracenyl complex **Ir2** being the least emissive (quantum yield (ϕ_{em}) < 2%), and complexes **Ir3** and **Ir8** (bearing 1,3-benzodioxole-5-yl and 1,4-benzodioxan-6-yl, respectively) being the most emissive (with ϕ_{em} > 25%, under the same conditions). We hypothesize that the radiative/non radiative decay ratio and phosphorescence lifetime differences observed across the **Ir2–Ir8** series may be associated with the different molecular rigidity and intramolecular interactions provided by the terpyridine ligand, which can impact the operative decay routes of the emissive ^{3}MLCT states.

In line with the above, the aggregation ability of these derivatives was studied by comparing the emission spectra in aerated DMSO : H_2O mixtures at constant concentration, using different water volume fractions (f_w). All complexes, except for **Ir2**, **Ir5** and **Ir8**, reach their maximum emission intensity at 30% water (Fig. 1C and S56). As the water content increases beyond 50%, a hypsochromic effect is observed, and once it exceeds 90%, the emission intensity drops to non-emissive levels. This behavior is attributed to an aggregation-caused quenching (ACQ) phenomenon, indicating that the new complexes are capable of forming aggregates.[61] However, complexes **Ir2** and **Ir5** exhibit distinct behavior: beyond 50% water content, a bathochromic shift is observed, accompanied by the emergence of a new narrow emission band centered at around 570 nm. This phenomenon could be attributed to an aggregation-induced emission (AIE) effect and may be facilitated by structural features such as extended π-conjugation or strong intermolecular π–π stacking interactions that restrict intramolecular motion in both complexes.[62]

Stability and photostability studies

As a critical factor for biological applications, the stability of the metal complexes was investigated. The compounds were dissolved in deuterated DMSO, and ^{1}H-NMR spectroscopy was employed to monitor any potential changes. No significant variations were observed after 48 h (Fig. S57–S64), indicating that the complexes remain stable in dimethyl sulfoxide. The stability of complexes **Ir1–Ir8** was subsequently evaluated in RPMI cell culture media (containing 5% DMSO) at 37 °C using UV/Vis spectroscopy. No appreciable changes were detected either, suggesting that complexes **Ir1–Ir8** exhibit high stability in cell culture media (Fig. S65). Additionally, considering their potential application in photodynamic therapy (PDT), the photostability of the complexes in DMSO was assessed by UV/Vis spectroscopy after irradiation with blue light (λ = 465 nm, 4.9 mW cm^{-2}) for a period of 2 h. However, under the previous conditions, no substantial differences are observed between the spectra of the complexes not exposed to light and those recorded upon 2 h of continuous irradiation (Fig. S66), thus indicating that the complexes are photostable for at least 2 h.

NADH photocatalytic oxidation

Subsequently, we investigated the influence of tuning the aryl substituent on ROS photogeneration by terpyridine Ir(III) complexes. NADH, a key electron source in the mitochondrial electron transport chain (ETC),[63] has emerged as a target for cancer drug development,[64] where it is converted to its oxidized form NAD^+. Disruptions in the NADH/NAD^+ ratio can inhibit ATP synthesis, depriving cancer cells of the energy required for proliferation. This ratio is therefore critical for cellular metabolism.[31] Fig. 2A and S67 show the UV/Vis spectra of NADH (100 μM) in the presence of each Ir complex (5 μM) in PBS (Phosphate-buffered saline, containing 5% DMF), recorded at different times after irradiation with blue light (λ = 465 nm, P = 4.6 mW cm^{-2}). In all cases, a gradual decrease in the characteristic absorbance of NADH is observed at approximately 339 nm, resulting from its photooxidation to NAD^+. The photooxidation is also evidenced by the increase in the absorbance of the NAD^+ band at *ca.* 259 nm.

To confirm that the oxidation was photocatalyzed solely by the **Ir1–Ir8** complexes in the presence of light, NADH was incubated with each complex in the dark. No spectral changes were

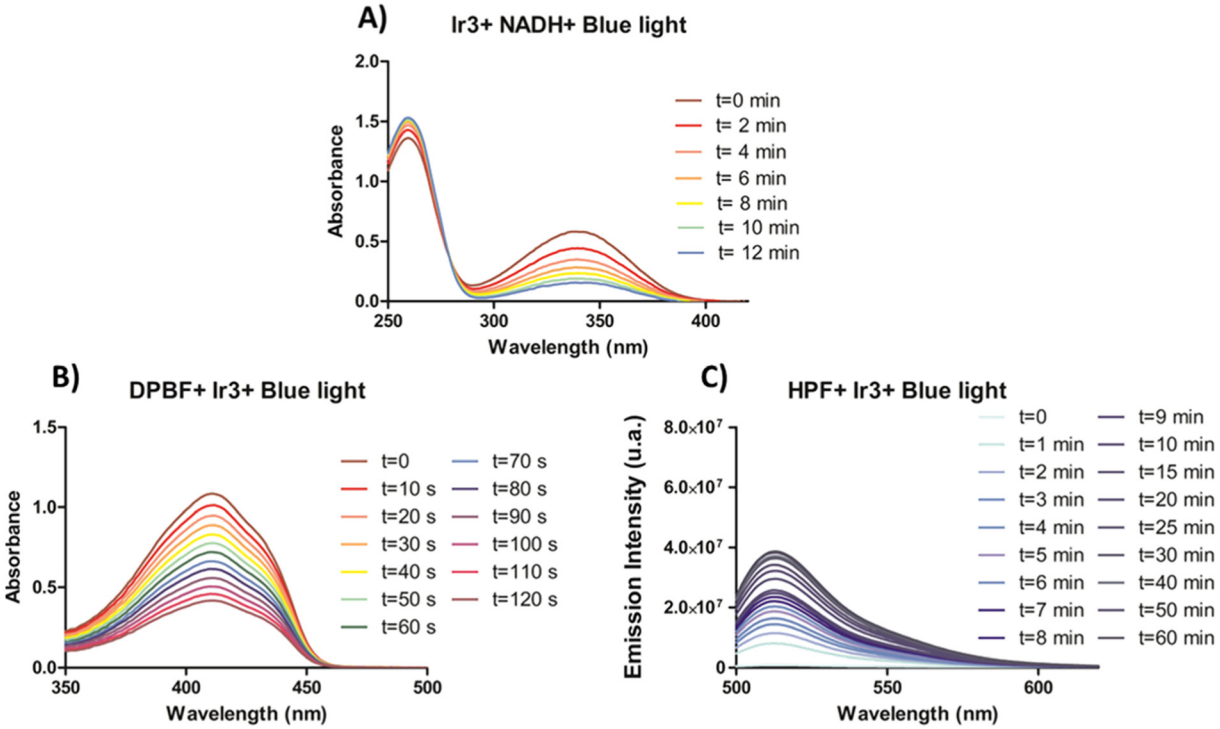

Fig. 2 (A) UV/Vis spectra of the NADH (100 μM) photo-oxidation catalyzed by **Ir3** (5 μM) in PBS (5% DMF) under blue light irradiation (λ = 465 nm, P (power) = 4.6 mW cm^{-2}). (B) UV/Vis spectra of DPBF (50 μM) in the presence of **Ir3** in acetonitrile under blue light irradiation at different times for a total of 2 min (λ = 465 nm, P = 0.48 mW cm^{-2}). (C) Emission spectra (recorded at λ_{exc} = 490 nm) of HPF (10 μM) in the presence of **Ir3** (10 μM) in PBS (5% DMF) when irradiated with blue light (λ = 465 nm, P = 4.7 mW cm^{-2}) at different times for 1 h.

observed after one hour (Fig. S68). Likewise, irradiating NADH in the absence of the complexes with blue light had no effect (Fig. S69). Thus, NADH photo-oxidation requires both blue light and the presence of **Ir1–Ir8**. Turnover number (TON) and turnover frequency (TOF) values were obtained to quantify the efficiency of the photo-oxidation process (Table S10). The 1,4-benzodioxan-6-yl terpy complex, **Ir8**, presents the highest TON and TOF values (15.44 and 112.29 h^{-1}, respectively), while complexes with 9-anthracenyl and 1-naphthyl substituents, **Ir2** and **Ir6**, exhibited the lowest values. NADH photo-oxidation was repeated under identical conditions with ROS scavengers: mannitol (20 mM) for hydroxyl radicals and sodium azide (10 mM) for singlet oxygen (Fig. S70 and S71). As shown in Table S10, the TON and TOF generally decreased, except for **Ir8**, whose TOF increased from 112.29 h^{-1} to 167.07 h^{-1} with mannitol. Complexes **Ir1–Ir7** thus operate *via* dual type I/II pathways, whereas **Ir8**—the most efficient photocatalyst—showed enhanced activity when hydroxyl radical formation was suppressed but a marked TOF decrease with sodium azide, indicating type II predominance.

The NADH photocatalytic oxidation was also studied by means of multiscale quantum mechanics/molecular mechanics (QM/MM) methods run with Amber[65] software, in combination with Terachem.[66–69] Each **Ir2**, **Ir3**, and **Ir8** molecule (the most active compounds of the series) was embedded in an octahedral water box in the presence of a NADH molecule (Fig. 3a) and simulated for 2 microseconds through classical molecular dynamics (MD). Metal complexes were described with easyPARM-derived force-field parameters,[70] while NADH was described with the OL21 DNA force field[47] and other parameters retrieved from the literature.[71,72] Analysis of the simulations reveals efficient and persistent non-covalent interactions, driven mainly by π-stacking and hydrogen bonding, as shown in Fig. 3b. The probability of finding both molecules forming a non-covalent heterodimer (distances between 5 and 10 Å) in water solution is overwhelmingly larger than the states in which both molecules are separated, as shown in Fig. S72. **Ir2** seems to exhibit the most efficient interactions, probably due to the extended aromatic system of the anthracene moiety, which facilitates π-stacking.

Fig. 3 shows the analysis of the charge of NADH in the S_0 ground and T_1 states along the MD simulation. In S_0, the Ir(III) complex and NADH have a molecular charge of +1 and −2, respectively, as shown in panel (a) for the three **Ir2**/NADH, **Ir3**/NADH, and **Ir8**/NADH systems. However, in the lowest-energy triplet excited state T_1, the charge distribution can change depending on the nature of the excitation, which is in turn modulated by the nuclear coordinates disposition as a function of temperature and other environmental perturbations such as solvent effects. Ir(+1)/NADH(−2) is indicative of local excitation, whereas Ir(0)/NADH(−1) or Ir(+2)/NADH(−3) indicates NADH → Ir and Ir → NADH charge transfer states, respectively. Fig. 3b evidences a significant fraction of snapshots in which the NADH → Ir charge transfer is the most stable state. This happens for the 20.2, 26.5, and 35.0% of the

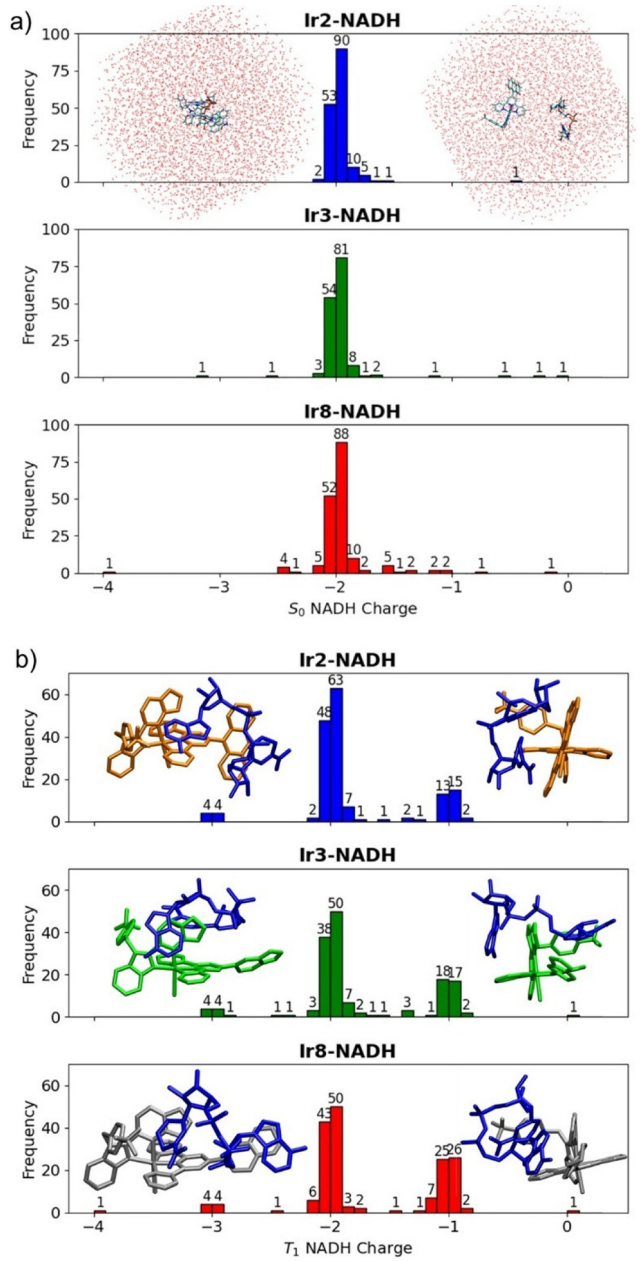

Fig. 3 Histogram of NADH Mulliken charges at the S_0 ground state (panel a) and T_1 excited state (panel b) for an ensemble of snapshots extracted from the MD simulations. The total sampling for each Ir(III) complex/NADH system is 163 frames for **Ir2**/NADH, 155 frames for **Ir3**/NADH, and 177 frames for **Ir8**/NADH. The **Ir2**/NADH system embedded in an octahedral water box with short (left) and long (right) distances between the metal complex and NADH is shown at the top of panel a. Panel b shows different side views of **Ir2** (orange), **Ir3** (green), and **Ir8** (silver) non-covalent heterodimers with NADH (blue), respectively. H atoms are omitted for the sake of clarity.

total number of snapshots analyzed for **Ir2**/NADH, **Ir3**/NADH, and **Ir8**/NADH, respectively, clearly indicating that **Ir8** is the photosensitizer that stabilizes the NADH → Ir states most efficiently. In turn, this correlates with a more efficient NADH photocatalysis.

The study of the T_1/S_0 energy difference along the MD snapshots (Fig. S73) shows that the most abundant energy gap is between 2 and 3 eV (620 and 413 nm, respectively) for the three Ir/NADH systems considered. All in all, the MD-QM/MM study unambiguously indicates that NADH → Ir charge transfer states are sufficiently stable to be populated after light absorption in a statistically significant number of configurations, representing the first step of the NADH photooxidation. Among the three **Ir2**, **Ir3**, and **Ir8** systems, the latter is deemed the most efficient photocatalyst, in good agreement with the experimental findings.

Evaluation of ROS photogeneration in cell-free media

Next, the ability of **Ir1–Ir8** to photogenerate ROS in cell-free media was investigated to determine whether type I, type II, or both types of ROS were produced. Firstly, the generation of singlet oxygen ($^1O_2$, type II ROS) was assessed by the decrease in 1,3-diphenylisobenzofuran (DPBF) absorbance at 411 nm, as DPBF reacts with singlet oxygen to form a colorless product.[58] Upon light irradiation (λ = 465 nm, P = 0.48 mW cm^{-2}), a gradual decrease in the DPBF absorbance peak (λ = 411 nm) was observed (Fig. 2B and S74), confirming the production of $^1O_2$. Fig. S75 presents a comparative analysis of the singlet oxygen ($^1O_2$) generation efficiency among **Ir1–Ir8** complexes. It reveals that **Ir2**, which features a 9-anthracenyl group on the tpy ligand, exhibits the highest singlet oxygen quantum yield (~77%). This value significantly exceeds those of the other Ir-tpy compounds synthesized in this study, whose yields ranged between 20% and 40% (Table S11).

After proving that **Ir1–Ir8** complexes generate singlet oxygen, we evaluated their ability to produce hydroxyl radicals OH$^\bullet$, using a spectroscopic method based on the oxidation of the almost non-fluorescent hydroxyphenyl fluorescein (HPF).[2,14] Upon blue light irradiation, all complexes (10 μM) were able to oxidize HPF (10 μM), resulting in bright green fluorescence. As shown in Fig. 2C and S76, all complexes significantly enhance OH$^\bullet$ production under blue light irradiation for one hour (λ = 465 nm, P = 4.7 mW cm^{-2}). For comparison, Fig. S77 highlights that **Ir7** and **Ir8** generate the highest amounts of OH$^\bullet$. Conversely, the terpyridine complex **Ir3**, containing the 1,3-benzodioxole-5-yl substituent, leads to a marked reduction in hydroxyl radical production under the same conditions. Overall, these results confirm the capacity of the new Ir(III) complexes to photogenerate both type I and type II ROS.

The feasibility of type I electron-transfer reactions between **Ir2**, **Ir3** and **Ir8** complexes and molecular oxygen leading to the generation of highly reactive superoxide species has been explored by computing the vertical electron affinity (VEA) and ionization potential (VIP) values of the involved species (Table 1). With the same approach, the electron transfer possibilities involving NADH and the Ir complexes were also considered to compare with the results presented in Fig. 3. Thermodynamic data indicate that the photoinduced electron transfer from one excited PS molecule to another PS molecule in the ground state is favorable either in T_1 or S_1 (reactions (1)

Table 1 Thermodynamics [ΔE = E(products) − E(reactants)] of type I PDT reactions based on the VEA and VIP values shown in Table S12

#	Type I photoreactions	Ir2	Ir3	Ir8
	Autoionization reactions			
(1)	$^3Ir^+ + {}^1Ir^+ \rightarrow {}^{\bullet}Ir^{2+} + {}^{\bullet}Ir$	0.58	0.54	0.52
(2)	$(^1Ir^+)^* + {}^1Ir^+ \rightarrow {}^{\bullet}Ir^{2+} + {}^{\bullet}Ir$	0.05	0.46	0.45
(3)	$^3Ir^+ + {}^3Ir^+ \rightarrow {}^{\bullet}Ir^{2+} + {}^{\bullet}Ir$	−1.39	−1.97	−2.01
	Indirect reaction			
(4)	$^{\bullet}Ir + {}^3O_2 \rightarrow {}^1Ir^+ + {}^{\bullet}O_2^-$	−0.27	−0.56	−0.56
	Direct electron transfer			
(5)	$^1Ir^+ + {}^3O_2 \rightarrow {}^{\bullet}Ir^{2+} + {}^{\bullet}O_2^-$	2.28	2.99	2.98
(6)	$^3Ir^+ + {}^3O_2 \rightarrow {}^{\bullet}Ir^{2+} + {}^{\bullet}O_2^-$	0.31	−0.02	−0.04
	Reactions with NADH			
(7)	$NADH^{2-} + {}^3Ir^+ \rightarrow {}^{\bullet}NADH^- + {}^{\bullet}Ir$	−0.19	−0.44	−0.46
(8)	$NADH^{2-} + {}^1Ir^+ \rightarrow {}^{\bullet}NADH^- + {}^{\bullet}Ir$	1.78	2.07	2.07
(9)	$^{\bullet}Ir + NADH^{2-} \rightarrow {}^1Ir^+ + NADH^{3-}$	1.72	1.43	1.43

All energies are in eV.

and (2), respectively). In contrast, all Ir complexes can undergo reduction in their triplet states *via* autoionization (reaction (3) in Table 1), with the net electron transfer being strongly exothermic. Moreover, the exothermicity increases markedly from **Ir2** to **Ir8**, in agreement with the experimental measurements. The subsequent electron transfer from the reduced form of the complexes ($^{\bullet}$Ir) to molecular oxygen *via* reaction (4) appears feasible in all cases, with a notably enhanced driving force for **Ir3** and **Ir8**, which exhibit the most negative values. The latter two complexes also show a slightly favorable process for direct electron transfer *via* reaction (6) in the triplet state, while it is clearly unfeasible in the ground state due to the high endothermicity predicted by reaction (5).

The direct reduction of the Ir complexes by $NADH^{2-}$ is favorable through the triplet-state species (reaction (7), Table 1). Notably, the exothermicity of this process increases progressively from **Ir2** to **Ir8**, aligning well with both experimental and QM/MM findings discussed above. The NADH → Ir charge transfer is unfeasible without light absorption, as quantified by reaction (8). The opposite Ir → NADH charge transfer pathway is not favourable even when considering the reduced form of the Ir complex examined *via* reaction (9), since it proves to be largely endothermic. A schematic sketch of the possible photocatalytic mechanism, partly based on previous works, is proposed in Fig. S78.

Antiproliferative activity

The antiproliferative potential of the novel iridium complexes was studied in three distinct human cancer cell lines: HeLa (cervix), HCT116 (colon), and A375 (melanoma), selected based on the irradiation compatibility of their anatomical sites in the clinic. The evaluation was conducted under both dark conditions and after exposure to blue light (420 nm). The results, presented in Table 2, outline the antiproliferative efficacy as determined by the MTT assay. The MTT assay is a widely used colorimetric technique for assessing cell viability, proliferation, and cytotoxicity, relying on the ability of mitochondrial enzymes in viable, active cells to reduce the tetrazolium dye MTT into formazan crystals.

Iridium complexes demonstrated strong antiproliferative effects across all tested cancer cell lines under irradiation. Their IC_{50} values fell within micromolar to submicromolar ranges, underscoring their high effectiveness in targeting malignant cells. Notably, some of the tested iridium complexes show a high phototoxicity index (PTI). All investigated iridium compounds are significantly more toxic when exposed to light compared to dark conditions. However, it is difficult to compare the photopotentiation efficiency within the group of Ir complexes as their low dark activity (an advantage for potential use in PDT) does not allow for the determination of precise IC_{50} values. Due to limited solubility, it was not possible to use concentrations higher than 200 μM. Nevertheless, of all the compounds tested, complexes **Ir2**, **Ir3**, and **Ir8** showed the highest phototoxic indices across all cancer cell lines.

Another significant and intriguing observation from Table 2 is the notably low activity in normal, non-cancerous cells (MRC5pd30, derived from human fetal lung fibroblasts) under dark conditions. This approach assumes a treatment scenario for a patient with a tumor in which irradiation is applied exclusively to the tumor site, leaving the surrounding healthy tissue unaffected by light. We calculated the selectivity

Table 2 Antiproliferative activity (IC_{50} values) evaluated using the MTT assay[a]

	HELA			HCT116			A375			MRC5PD30 (normal)			
	Dark	420 nm[b]	PTI[c]	Dark	420 nm[b]	PTI[c]	Dark	420 nm[b]	PTI[c]	$Dark_{2\ h}$	SI[d]	$Dark_{72\ h}$	SI[d]
IR1	>200	8.3 ± 0.3	>24	>200	3.8 ± 0.2	>53	>200	5 ± 1	>43	>200	>35	22 ± 5	4
IR2	10 ± 2	0.14 ± 0.04	69	3.5 ± 0.9	0.026 ± 0.003	135	2.7 ± 0.9	0.037 ± 0.005	72	12 ± 2	177	3.0 ± 0.1	44
IR3	>200	0.9 ± 0.2	>217	19 ± 4	0.14 ± 0.03	136	109 ± 17	0.50 ± 0.08	218	68 ± 18	130	10 ± 2	19
IR4	>200	10 ± 1	>20	>200	4 ± 1	>50	>200	10 ± 2	>20	>200	>25	11 ± 1	1.4
IR5	>200	2.2 ± 0.2	>91	11 ± 1	1.08 ± 0.09	10	45 ± 6	1.7 ± 0.4	26	150 ± 19	90	15 ± 3	9
IR6	10 ± 1	0.7 ± 0.2	14	3.1 ± 0.7	0.14 ± 0.03	22	2.2 ± 0.3	0.32 ± 0.09	7	11 ± 2	27	3.4 ± 0.2	6
IR7	>200	5.2 ± 0.9	>38	>200	3.2 ± 0.2	>63	>200	4 ± 1	>46	>200	>47	90 ± 10	21
IR8	>200	1.3 ± 0.5	>158	19 ± 4	0.16 ± 0.05	119	112 ± 9	0.6 ± 0.1	187	68 ± 15	99	10 ± 3	15

[a] Cells were pretreated for 1 h in EBSS (Earle's Balanced Salt Solution), followed by either irradiation at 420 nm for 1 h or maintenance under dark conditions. After treatment, EBSS was removed, and fresh culture medium was added. The cells were then allowed to recover for 70 h. Final viability was determined using the MTT assay. [b] IC_{50} values for irradiated samples; the untreated irradiated control was set to represent 100% cell viability. [c] PTI (phototoxicity index) = $IC_{50(dark)}/IC_{50(420\ nm)}$. [d] SI (selectivity index) = $IC_{50(dark,MRC5)}$/average $IC_{50(420\ nm,Hela,HCT116,A375)}$.

indices as the IC_{50} in non-cancerous non-irradiated cells divided by the average IC_{50} in irradiated cancer cells. The SI indices indicate how much more effective a drug is against cancer cells compared to its toxicity toward healthy cells. A higher SI value indicates greater selectivity.

To evaluate the long-term impact of the iridium complexes on non-cancerous human MRC5pd30 cells, we cultured the cells with the iridium complexes for 72 h. Subsequently, we measured their viability using the MTT assay. The IC_{50} values observed after this prolonged exposure significantly differed from those obtained after a 2 h treatment followed by a 70 h recovery in a drug-free medium. This variation is primarily due to the slow proliferation rate of MRC5pd30 cells, which originate from normal fetal lung tissue and exhibit normal growth control. Detecting the antiproliferative effects of the studied compounds requires a more extended exposure period in these cells, indicating that the investigated iridium complexes do not cause acute toxicity in MRC5pd30 non-cancerous cells. This is advantageous since agents that induce immediate cell damage tend to be highly toxic.

In previous studies,[73,74] some iridium complexes have been shown to disrupt mitochondrial function, potentially interfering with the reduction process in MTT. This disruption could lead to misleading results – cells may appear non-viable even if they remain alive but metabolically impaired. To address this issue, we employed an alternative sulforhodamine (SRB) assay, which quantifies the cellular protein content, for selected complexes **Ir2** and **Ir3** in HCT116 cells (Table S13). The IC_{50} values obtained from the SRB assay were consistent with the data from the MTT assay. These findings confirm that the tested Ir complexes do not impair mitochondrial function in a manner that would compromise the reliability of the MTT results.

Cellular accumulation

To determine the permeability and accumulation of the new iridium complexes in the cells, we conducted an experiment measuring the amount of iridium inside the HCT116 cells. Cells were exposed to the studied complexes at their equimolar concentrations (5 μM) for 2 h in the dark, then washed, harvested, counted, and immediately digested in hydrochloric acid. The final amount of iridium inside the cells was evaluated by ICP-MS (Table 3).

For further biological studies, the two iridium complexes, **Ir2** and **Ir3**, were selected based on their superior results in antiproliferative activity and selectivity screening (mainly due to their high PTI, in the range of 69–>217); HCT116 cells were employed in these studies, as they proved to be the most sensitive to the two Ir-complexes.

Table 3 Intracellular accumulation of Ir in HCT116 cells (ng Ir per 10^6 cells)

Ir1	Ir2	Ir3	Ir4	Ir5	Ir6	Ir7	Ir8
59 ± 13	131 ± 21	102 ± 20	89 ± 2	74 ± 9	112 ± 9	88 ± 4	103 ± 1

Cellular localization

Beyond the mere penetration and accumulation of the drug within the cell, its intracellular distribution plays a pivotal role in determining its mechanism of action. Therefore, using a confocal microscope (Leica SP5), we investigated the cellular localization of the selected iridium complexes (**Ir2** and **Ir3**) in a 2D cell culture of HCT116 cancer cells (Fig. 4).

Only a weak fluorescence signal was detected for complex **Ir2** under the used conditions. In contrast, a stronger signal was observed for complex **Ir3**. Importantly, localization studies revealed that the Ir complexes are predominantly situated in the cytoplasm, with no detectable presence in the cell nucleus.

For better identification of the intracellular localization of the Ir complexes, colocalization experiments were conducted. The data revealed no overlap between the fluorescence signal of **Ir3** and markers of mitochondria or the endoplasmic reticulum (Fig. S79), with Pearson's correlation coefficients of 0.12 ± 0.03 and 0.08 ± 0.02, respectively. Rather than associating with specific organelles, **Ir3** appears to be diffusely distributed throughout the cytoplasm; a few brighter spots may correspond to aggregates of **Ir3**. In the cytoplasm, the agents can interact with cellular components that regulate cell death or proliferation.

Cellular morphology

During localization studies using a confocal microscope, we observed an intriguing phenomenon: the cellular morphology changed significantly within a very short time. After irradiation of the cells treated with **Ir3** with an excitation laser (355 nm), small membrane blebs appeared within 5–10 min (Fig. 5A). It is essential to note that this effect was not observed in untreated cells, even when they were irradiated with the same laser setup. When the morphology was monitored for a more extended period (1–24 h), another morphological alteration became evident, such as cytoplasmic vacuolization, where the vacuoles filled almost the entire cell volume (Fig. 5B). The whole cells were swollen and rounded. These morphological features indicate the oncotic-like cell death. Oncosis is a form of cell death, characterized by significant energy consumption, cell swelling, dilation of the endoplasmic reticulum, mitochondrial swelling, and nuclear chromatin aggregation.[75]

Cell death: annexin V/propidium iodide

It has been shown that oncotic cells exhibit annexin V positivity, similar to apoptotic cells. Typically, phosphatidylserine residues are located on the inner side of the cytoplasmic membrane. However, during oncosis, these residues are externalized. This externalization is not an early event in oncosis, but occurs as cells progress toward loss of membrane integrity. Externalized phosphatidylserine can be recognized by annexin V. This was also observed for HCT116 cells treated with complexes **Ir2** or **Ir3** (Fig. 6A). After irradiation and a 24 h recovery

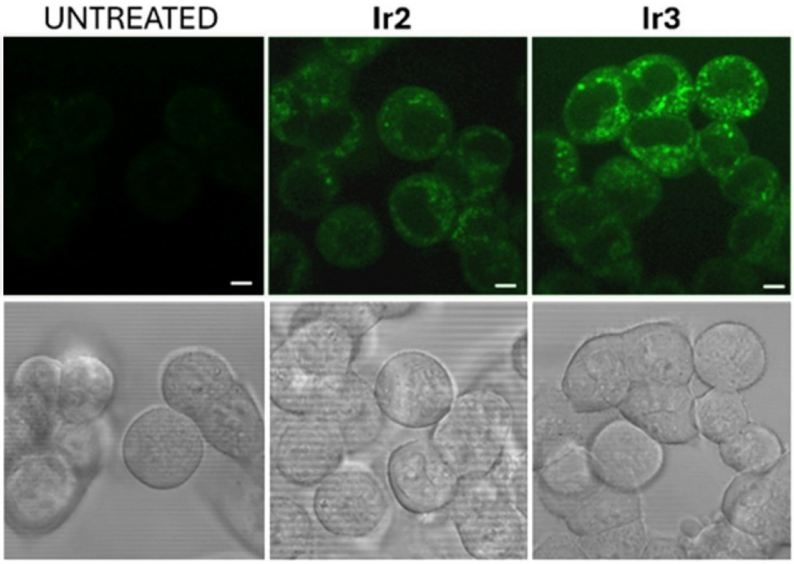

Fig. 4 Cellular localization of Ir complexes analyzed using a confocal microscope. HCT116 cells were seeded on confocal dishes and treated with **Ir2** or **Ir3** (0.5 μM) for 3 h under dark conditions. Immediately, live cell imaging was performed using a confocal microscope. Confocal images were captured using a UV laser ($\lambda_{ex}/\lambda_{em}$ = 355/400–485 nm), and the image was taken immediately. Top panels: fluorescence from the iridium complexes. Bottom panels: bright field. Scale bars represent 5 μm.

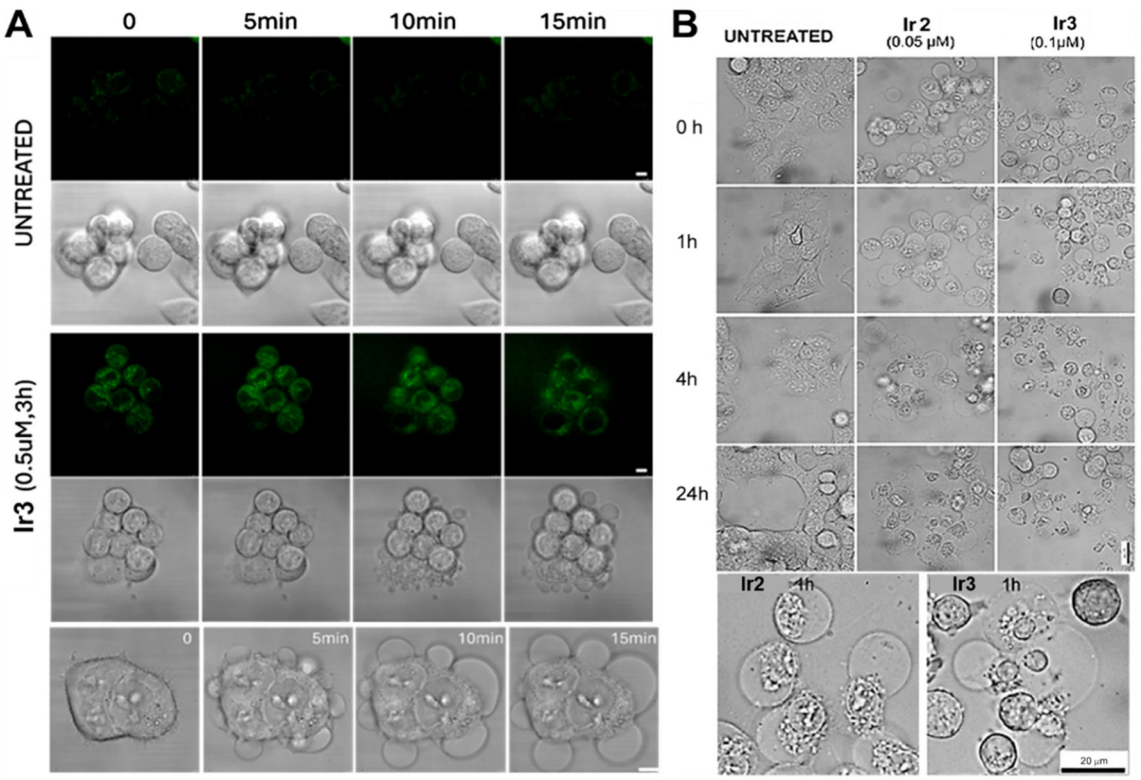

Fig. 5 A. HCT116 cell morphology monitored using a confocal microscope (Leica SP5). HCT116 cells were treated with **Ir3** (0.5 μM) for 3 h in DMEM (Dulbecco's modified Eagle's medium) (without phenol red). The cells were directly analyzed under the microscope, where they were irradiated with a laser (355 nm, 75%) to monitor the fluorescence signal of the Ir complex. However, the irradiation was sufficient to activate the Ir complex, and immediate oncotic-like cell death was observed within 5 min after irradiation. Scale bar: 5 μm. B. Morphology of HCT116 cells. Cells were pretreated with **Ir2** (0.05 μM) or **Ir3** (0.1 μM) for 1 h in EBSS, irradiated (420 nm) for 1 h. After this treatment procedure, the EBSS was removed, and fresh culture medium was added. The cellular morphology was monitored at 0, 1, 4, and 24 h after irradiation using an inverted microscope. Scale bars: 20 μm.

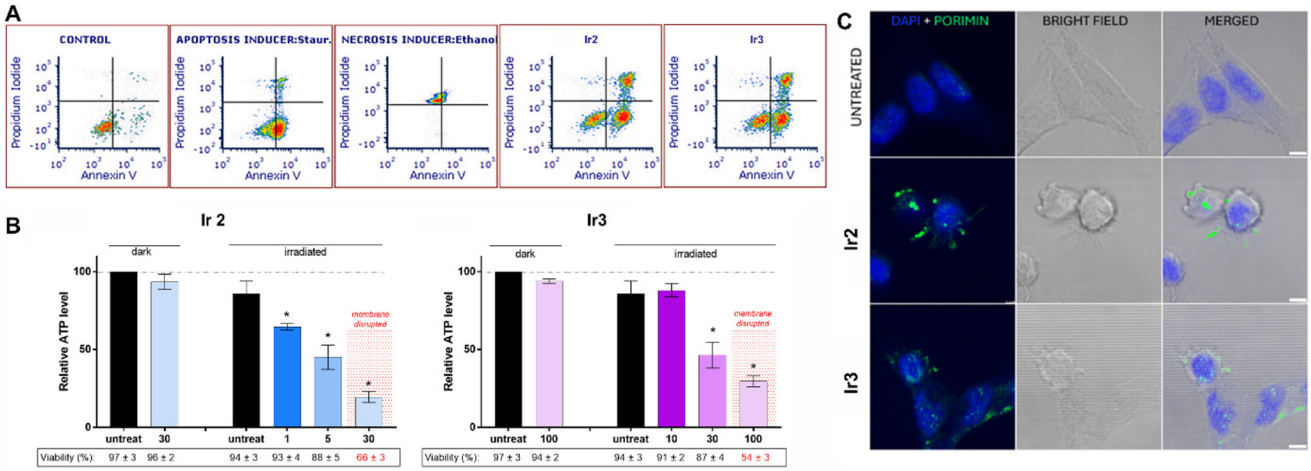

Fig. 6 A. Flow cytometric analysis of HCT116 cells stained with annexin V/propidium iodide assay (for details, see the Experimental section). B. Intracellular ATP levels in HCT116 cells treated with **Ir2** (left) at concentrations of 1, 5 and 30 nM or **Ir3** (right) at concentrations of 10, 30, and 100 nM, or untreated. After 1 h of pretreatment, the cells were either irradiated (420 nm, 1 h) or kept in the dark. Cells were then incubated in a drug-free medium for 1 h. Intracellular ATP levels were determined using the CellTiter-Glo reagent (Promega). Cell membrane integrity was evaluated by the Trypan blue exclusion assay. Statistical significance: $p \leq 0.01$. C. Immunofluorescence staining of HCT116 cells, untreated or treated with **Ir2** or **Ir3** (concentration corresponding to IC_{50}) and irradiated with blue light, showing membrane localization of porimin (green fluorescence signal). The nuclei of the cells are stained with DAPI. Scale bar: 5 μm.

period, the annexin V-positive populations were clearly observable.

Annexin V positivity is often associated with apoptosis; therefore, the importance of combining annexin V assays with morphological criteria and other markers to accurately distinguish between apoptosis and oncosis is emphasized. Although distinct pathways mediate apoptosis and necrosis, they share overlapping involvement of cell surface death receptors, mitochondria, and the endoplasmic reticulum. Oncosis is characterized by the early opening of MPTP (mitochondrial permeability transition pore) in the inner membrane, occurring without the release of cytochrome c. The initiation of MPTP results in rapid loss of the mitochondrial membrane potential ($\Delta\Psi_m$), interruption of ATP synthesis, solute influx, and mitochondrial swelling.[75] Unlike apoptosis, oncosis does not involve the activation of caspases or the formation of apoptotic bodies. A surface receptor, porimin (pro-oncosis receptor inducing membrane injury), is considered an indicator of oncotic cell death.

ATP depletion

ATP plays a critical role in oncosis. Unlike apoptosis, which is an energy-independent process, oncosis occurs when cells fail to maintain the ionic balance due to insufficient ATP, resulting in uncontrolled water influx and cellular swelling. Oncotic inducers contribute to a decline in ATP concentration, further driving this process.

In our work, when HCT116 cells were treated with **Ir2** or **Ir3** and irradiated, their ATP level showed a rapid reduction compared to untreated, non-irradiated cells. The effect was evident even at low Ir complex concentrations (1, 5 nM for **Ir2** and 30 nM for **Ir3**) within a short time interval (1 h), while the majority of the cell population still maintained membrane integrity (Fig. 6B).

Porimin staining

A surface receptor, porimin (pro-oncosis receptor inducing membrane injury), is a key marker and mediator of oncosis. Porimin plays a crucial role in the oncotic process by facilitating membrane permeability changes, leading to the characteristic swelling of the entire cell during oncosis and cell lysis. The increased expression of porimin is associated with mitochondrial dysfunction and ROS accumulation, which further drives oncosis. As shown in Fig. 6C, an elevated expression of porimin upon incubation with **Ir2** or **Ir3** and subsequent irradiation was demonstrated by confocal microscopy.

ROS production

Since ROS can be generated rapidly upon irradiation of treated cells, this process is challenging to capture. To address this issue, we designed an experiment where cells were first pretreated with complexes **Ir2** or **Ir3**, followed by the introduction of the CellROX marker just before irradiation. The cells were then irradiated for 10 min, allowing us to use shorter time intervals and successfully capture ROS, which can form very quickly but are also rapidly processed within the cells.

Blue light irradiation itself may induce reactive oxygen species (ROS) in cells,[76,77] leading to an increased oxidation of CellROX dyes and a stronger fluorescence signal. This is evident in Fig. 7A, where untreated cells (black column) exhibit an increased level of intracellular ROS, even after 10 min of blue light irradiation. However, the increased production of ROS in the untreated control does not appear to affect the overall cell viability. When comparing MTT data for

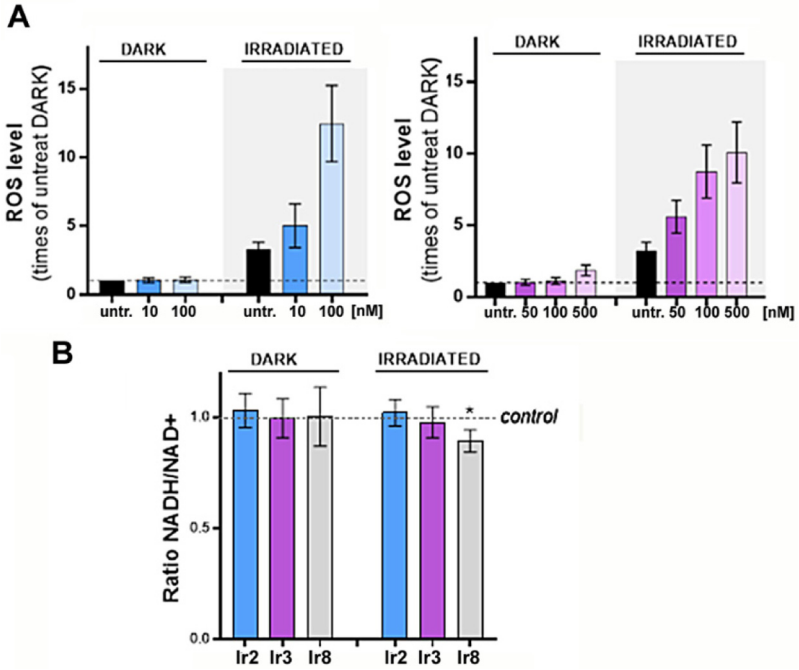

Fig. 7 A. Intracellular ROS production. HCT116 cells were treated with complexes **Ir2** (left) or **Ir3** (right). After 30 min, the CellROX Green dye was added (at a final concentration of 2.5 μM). After 30 min, the EBSS with the complex and dye was removed, cells were washed, and drug-free EBSS was added. Cultures were irradiated with blue light (10 min). Immediately after irradiation, the cells were harvested and analyzed using a flow cytometer Amnis. B. NADH/NAD^+ ratio determined using an NAD^+/NADH assay kit (Sigma-Aldrich). HCT116 cells were treated with complexes **Ir2** (5 nM), **Ir3** (30 nM), or **Ir8** (30 nM). The selected concentrations correspond to levels at which the cell membrane is not disrupted and the cells exhibit at least 90% viability. Cell membrane integrity was evaluated by the Trypan blue exclusion assay. After 1 h pretreatment, the cells were either irradiated (420 nm, 1 h) or kept in the dark. Cells were then incubated in a drug-free medium for 1 h. Intracellular NADH and NAD^+ levels were determined using the NAD^+/NADH assay kit (Merck) according to the manufacturer's instructions. Statistical significance: * $p \leq 0.01$.

dark and irradiated controls, we found no significant differences (not shown).

In cells pretreated with complexes **Ir2** or **Ir3**, we observed a significantly higher ROS production compared to untreated (irradiated-only) cells (Fig. 7A). As a result, the most significant increase in ROS occurs within a short irradiation time in the presence of the Ir complexes.

To demonstrate the relationship between ROS production and the observed photobiological activity and confirm the involvement of ROS in the phototoxicity of complexes **Ir2** and **Ir3**, the effects of various ROS inhibitors and scavengers on the phototoxic response of the Ir complexes after irradiation were evaluated. It was verified that the individual scavengers at the concentrations used did not affect the cell viability compared to the control incubated in the complex-free medium.[78] The results are summarized in Fig. S80.

The effect of irradiated Ir was inhibited in the presence of the hydroxyl radical ($OH^{\bullet}$) scavenger, mannitol, as well as in the presence of sodium azide, a potent singlet oxygen quencher. This suggests that these types of radicals participate in the biological activity of the studied Ir complexes, in accordance with the results obtained in the non-cellular environment, where the formation of OH radicals and singlet oxygen under irradiation was demonstrated. Thus, the above-described findings indicate that the photopotentiation of both **Ir2** and **Ir3** is associated with ROS generation and that the resulting oxidative stress plays a role in their phototoxic effects.

Considering that the Ir complexes investigated in this study also exhibited a certain degree of dark toxicity, albeit relatively low (Table 2), additional experiments were performed to elucidate the mechanism underlying their biological activity in the absence of irradiation. The results showed that, at concentrations corresponding to their dark IC_{50} values, ROS levels in the treated HCT116 cells increased above the level observed in untreated control cells, with a more pronounced rise observed for **Ir3** (Fig. S81A). Furthermore, experiments employing ROS scavengers demonstrated that quenching ROS reduces the overall biological effect of both complexes in the dark, indicating that ROS generation contributes to the dark biological activity of **Ir2** and **Ir3** (Fig. S81B). Nonetheless, other factors, such as potential interactions with specific molecular targets, cannot be excluded as contributors to the dark toxicity. However, given that the primary focus of this study is the light-induced activation of the investigated complexes, a detailed elucidation of the mechanisms responsible for dark toxicity lies beyond the scope of the present work.

NADH/NAD^+ ratio

Since the results obtained from spectrophotometric measurements showed (Fig. 2A and S67) that the investigated Ir com-

plexes photooxidize NADH to NAD^+ in a cell-free medium, we tested whether this photocatalytic ability of the studied Ir complexes is also reflected in cells. In addition to complexes **Ir2** and **Ir3**, which we tested in all other experiments (due to good phototoxicity and high PI), we also included complex **Ir8** in this test, which showed the highest turnover frequency (TOF) in spectroscopic studies (Table S10), *i.e.*, making it the most effective catalyst.

The $NADH/NAD^+$ ratio serves as a key indicator of a cell's redox balance and energy metabolism. In healthy cells, this ratio is carefully maintained within a specific range, which can vary depending on the cellular compartment and cell type. It is tightly regulated and plays a central role in essential cellular functions.

We investigated the intracellular $NADH/NAD^+$ ratio after HCT116 cells were treated with complexes **Ir2**, **Ir3**, or **Ir8** and their photoinduction (Fig. 7B). The $NADH/NAD^+$ ratio was unaffected after incubation with the Ir complexes in the dark. On light irradiation, only **Ir8** induced a significant decrease in the $NADH/NAD^+$ ratio.

It is therefore reasonable to conclude that, in accordance with the spectroscopic results obtained in the cell-free medium (Fig. 2A and S67), where photooxidation did not occur in the dark, there is no difference in the $NADH/NAD^+$ ratio in cells. After irradiation, a small but statistically significant decrease in the $NADH/NAD^+$ ratio was observed only when the cells were treated with **Ir8** (the most effective photocatalyst, as predicted by the multiscale computational results shown in Fig. 3b), so it can be assumed that this may also partially contribute to its antiproliferative effects under blue light irradiation.

The mechanism proposed for the photocatalytic oxidation of NADH by Ir complexes involves the transfer of an electron from NADH to the Ir complex in its excited $^*Ir(III)$ state, followed by the formation of $O_2^{\bullet-}$ and the unstable $NADH^{\bullet+}$ intermediates. These transient species subsequently react to ultimately produce NAD^+ and H_2O_2.[32,79] As shown in Fig. S82, the intracellular concentration of H_2O_2 increased in cells treated with **Ir8** and exposed to irradiation compared to untreated cells or those kept in the dark. Moreover, the cellular H_2O_2 level was significantly reduced in the presence of pyruvate, a known H_2O_2 and superoxide radical scavenger,[80] confirming the effect of irradiated **Ir8** on hydrogen peroxide evolution in HCT116 cells.

To assess whether the decrease in the $NADH/NAD^+$ ratio found for cells treated with **Ir8** may be biologically relevant, additional experiments were performed. Changes in glucose consumption and lactate production have been quantified. The treatment of HCT116 cells with complex **Ir8** under the same conditions in which the alteration in the $NADH/NAD^+$ ratio was detected (Fig. 7B) resulted in a reduction of lactate secretion; while the amount of lactate produced by the untreated irradiated control was 2400 nmol mL^{-1} of medium, in the **Ir8**-treated and irradiated samples, the lactate production decreased to 1740 ± 30 nmol mL^{-1} of medium. The decrease in lactate production could be associated with inhibition of the reduction of pyruvate to lactate, a key reaction of glycolysis in which NADH acts as a reducing agent. Concurrently, we observed slightly reduced glucose consumption – 1.35 μmol per 10^5 cells for the untreated irradiated control compared to 0.75 μmol per 10^5 cells for the treated and irradiated with **Ir8** – and a pronounced decrease in intracellular ATP levels (Fig. S83).

It should be noted, however, that there is evidence that reactive oxygen species (ROS) can modulate the glycolytic flux in cancer cells *via* up-regulation of proteins in the glycolytic pathway.[81–83] As our work demonstrates that Ir complexes – particularly **Ir8** – exert dual modes of action, encompassing not only photocatalytic oxidation of NADH but also the classical PDT mechanisms of ROS generation *via* type I and type II pathways, interpretation of these results is challenging. The relative contributions of these mechanisms to the observed metabolic effects cannot be distinguished under the current experimental conditions.

Morphological changes in 3D spheroid cultures

Next, we examined morphological alterations in 3D tumor spheroids in response to drug-induced cytotoxicity. Compared with untreated viable tumor spheroids, after treatment with **Ir2**, morphological alterations are visible (Fig. 8A–C), including an irregular and uneven surface, a decrease in spheroid size, and a halo of cell debris or loosening. A defining feature of viable 3D spheroids is cell–cell contact, characterized by a cohesive, circular, or smooth surface. Loosening of cell–cell contacts, compactness, or spheroid integrity is a key defining feature of cytotoxic drug effects. The quiescent or dead cells in 3D spheroids, as observed under bright-field imaging, appear as the darkest, typically located in the center of the spheroid.

Cell viability in 3D spheroids

CellTiter-Glo® 3D cell viability assay. The CellTiter-Glo® 3D cell viability assay is a reagent developed by Promega for measuring the cell viability in 3D microtissue cultures. This reagent is specifically formulated to penetrate large spheroids and produce a luminescent signal that is finally measured.

Treatment of HCT116 spheroids with **Ir2** or **Ir3** demonstrated that both complexes were more active following blue light irradiation compared to dark conditions (Fig. S84). However, despite their increased activity upon irradiation, the phototoxicity index was lower than that observed for cytotoxicity in 2D cell cultures. This suggests that the overall phototoxic impact in spheroid models is reduced compared to traditional 2D cultures, possibly due to differences in the cellular architecture that limit drug and light penetration.

Therefore, confocal microscopy was used to assess the ability of the **Ir** complexes to penetrate the cell mass of the spheroid. As the low intrinsic fluorescence of **Ir2** (see Fig. S55 and Fig. 4) prevented reliable signal acquisition, the experiment was performed with **Ir3**. The spheroids from HCT116 (mean diameter 300 μm), formed over 4 days, were treated with **Ir3** (5 μM) for 4 h and the fluorescence signal was visualized (Fig. S85). The fluorescence intensity was quantitatively analyzed to determine the complex's

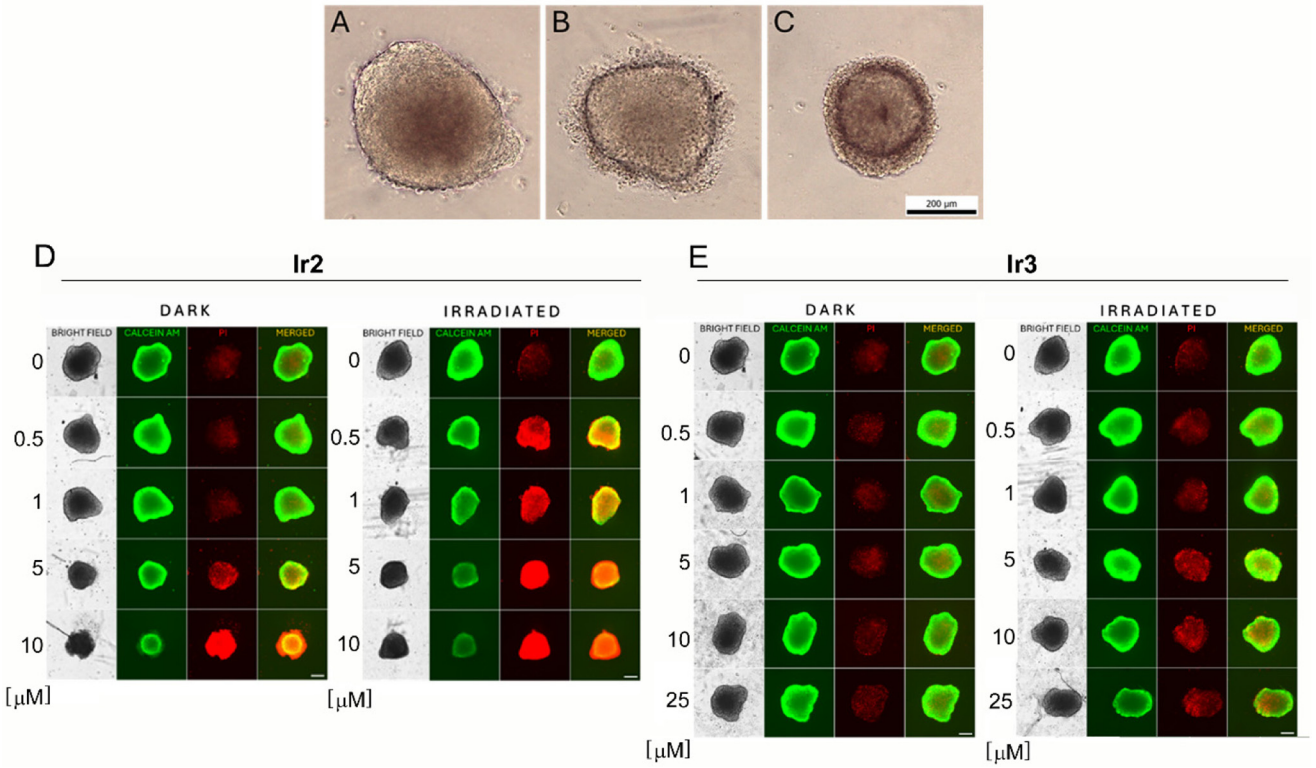

Fig. 8 (A–C) Morphological alterations in 3D tumor spheroids under bright field imaging. A. untreated, dark: viable tumor spheroid with a regular size and shape, compactness, integrity and smooth surface; B. **Ir2**, 0.5 µM, irradiated: a decreased spheroid size, uneven surface with halo of loosened cells or debris; C. **Ir2**, 5 µM, irradiated: quiescent or dead cells in 3D spheroids reflected as the darkest areas in the spheroid. (D and E) Representative images of HCT116 spheroids. HCT116 spheroids were treated with **Ir2** (D) or **Ir3** (E) for 1 h in the dark, followed by either 1 h of blue light irradiation (irradiated) or 1 h of incubation in darkness (DARK). Subsequently, EBSS was replaced with drug-free sphere-forming medium, and the spheroids were maintained in culture for 72 h. At the 72 h timepoint, HCT116 spheroids were stained with calcein AM (2 µM) and propidium iodide (8 µg mL^{-1}) for 2 h. Immediately after the staining, the plates were processed using the JuLi™ Stage Cell Recorder (NanoEntek, Germany) to capture fluorescence. Scale bar: 200 µm. For quantitative evaluation, see Fig. S86.

penetration depth (Fig. S85D). As indicated, the fluorescence signal was distributed unevenly, with the highest intensity in the periphery and the intermediate zone (approximately to a depth of 80 µm from the surface), whereas fluorescence in the spheroid core was low. This may indicate that, within the relatively short treatment period, the complex penetrated relatively deeply although it did not have sufficient time to penetrate the entire volume of the spheroid. However, it should also be noted that the observed effect (*i.e.*, low fluorescence in the spheroid center) may be related to the limited penetration of the excitation light into the dense cellular mass, as the light is strongly scattered and absorbed by the cells and the surrounding medium. This likely reduces the effective excitation intensity reaching the core, thereby decreasing the emitted fluorescence signal.

Consequently, given that the ability to penetrate tumor tissue represents a limiting factor that could restrict the potential use of the Ir complex for PDT, further efforts will be directed toward improving the penetration capabilities of this class of Ir complexes.

Spheroid calcein AM and PI staining. Propidium iodide (PI) is a fluorescent dye that is impermeable to live cells, meaning it only stains dead or membrane-compromised cells. It does not penetrate live cells and therefore does not provide a fluorescent signal. Simultaneously, with the increase in PI staining, a decrease in the fluorescence signal for calcein AM is observed. In contrast to PI, calcein AM marks live cells. Calcein AM is a non-fluorescent compound that can easily enter live cells due to its lipophilic properties. Once inside, intracellular esterases cleave the molecule, converting it into fluorescent calcein, which is retained within the cytoplasm. Only live cells retain fluorescence, making calcein AM useful for viability assays.

As shown in Fig. 8, irradiation of the spheroids pretreated primarily with **Ir2** resulted in a vast increase in PI fluorescence, indicating a substantial accrual of dead cells within the spheroid volume. A similar increase in PI fluorescence was also observed in non-irradiated samples; however, this effect was noticeable only at significantly higher concentrations of the Ir complexes (Fig. 8 and S86). Within the range of concentrations used in the experiment, the impact of **Ir2** was more pronounced compared to that of **Ir3**, in agreement with its lower IC_{50} value determined for 3D colonospheres (table in Fig. S84 and S87). On the other hand, complex **Ir3** exhibits lower dark toxicity yet maintains good PTI, which may be advantageous considering potential side effects.

Conclusions

We successfully synthesized and comprehensively characterized eight new arylterpyridine Ir(III) complexes **Ir1–8** with the general formula [Ir(N^N^N)(C^N)Cl]PF_6, where N^N^N is 4′-(aryl)-2,2′:6′,2″-terpyridine and C^N is deprotonated 2-(1,3-benzodioxol-5-yl)-1-(4-(trifluoromethyl)benzyl)-1*H*-benzo[*d*]imidazole. The ligands incorporated *para*-substituents (Cl, CF_3, CO_2Me, carbazolyl) or extended aromatic groups (benzodioxole, benzodioxane, naphthyl, anthracenyl). Upon irradiation with biocompatible blue light, these complexes exhibited potent antiproliferative effects in both 2D and 3D cancer cell models, while inducing minimal acute toxicity in non-cancerous cells. Among them, **Ir2**, **Ir3**, and **Ir8** were emphasized because each represents a distinctive photophysical/biological profile: **Ir2**, with its π-expanded scaffold, achieves the highest $^1O_2$ yield (~77%), the lowest IC_{50}, and the best selectivity index; **Ir3**, bearing electron-rich substituents, combines a high emission quantum yield with the highest phototoxicity indexes across cell lines; and **Ir8**, also electron-rich, exhibits the longest emission lifetime, the largest NADH photooxidation TOF, and pronounced $^{\bullet}OH$ generation, explaining its superior photocytotoxicity. These three complexes were therefore selected for further investigation.

Complexes **Ir2** and **Ir3** showed superior antiproliferative activity and selectivity, particularly against the HCT116 cell line, and confocal microscopy revealed that they localize predominantly in the cytoplasm. Light activation induced marked morphological changes consistent with oncotic-like cell death, confirmed by ATP depletion and porimin upregulation, indicating membrane injury.

Mechanistic studies revealed that **Ir2** and **Ir3** catalyzed NADH photo-oxidation with high turnover frequencies in aqueous solution and **Ir8** in cancer cells, accompanied by ROS generation. Molecular dynamics and hybrid QM/MM simulations further indicated the formation of non-covalent Ir–NADH heterodimers, with Mulliken charge analysis supporting NADH → Ir charge transfer as the most stable triplet state in a statistically relevant number of configurations. These computational findings align with experimental data, showing that **Ir8** (1,4-benzodioxan-6-yl) is the most efficient NADH photocatalyst, confirmed by intracellular NAD^+/NADH measurements in HCT116 cells.

Overall, **Ir2**, **Ir3**, and **Ir8** emerged as the most promising candidates, with their mechanism of action involving synergistic phototoxic and photocatalytic effects. These findings provide a mechanistic foundation for the development of innovative phototherapeutic strategies distinct from classical ROS-driven photodynamic therapy.

Author contributions

I. R.-C. contributed to experimental work, data curation, formal analysis, investigation, methodology, software, validation, and writing – review & editing. L. M. contributed to data curation, formal analysis, investigation, methodology, software, validation, and writing – review & editing. M. J. P.-M. contributed to conceptualisation, data curation, formal analysis, investigation, methodology, software, validation, and writing – review & editing. J. K. contributed to conceptualisation, data curation, formal analysis, investigation, methodology, software, validation, writing – original draft, and writing – review & editing. H. K. contributed to investigation. C. J. contributed to data curation, formal analysis, investigation, methodology, software, validation, writing – review & editing, and X-ray structure refinement and analysis of **Ir3**·0.5CH_2Cl_2. M. E. A. contributed to data curation, formal analysis, investigation, methodology, software, validation, and writing – review & editing. A. F.-M. contributed to conceptualisation, data curation, formal analysis, investigation, methodology, software, supervision, validation, writing – original draft, writing – review & editing, funding acquisition, and project administration. J. R. contributed to conceptualisation, formal analysis, investigation, methodology, supervision, writing – original draft, writing – review & editing, funding acquisition, project administration, and resources. V. B. contributed to conceptualisation, funding acquisition, project administration, resources, supervision, writing – original draft, and writing – review & editing.

Conflicts of interest

There are no conflicts to declare.

Data availability

The data supporting this article have been included as part of the supplementary information (SI). Supplementary information: instrumentation, methods, synthetic details of ligands **L2–L8**, proligand **HC^N**, iridium precursors **A1–A8**, iridium complexes **Ir1–Ir8**, characterisation, analytical and photophysical data, TD-DFT calculations, molecular dynamics and hybrid QM/MM simulations, the photochemical evaluation, the photo-(cytotoxic) experiments conducted and microscopy experiments. See DOI: **https://doi.org/10.1039/d5qi02205c**.

CCDC 2497678 contains the supplementary crystallographic data for this paper.[84]

Acknowledgements

The work of J. K. and V. B. was supported by the Czech Science Foundation (grant no. 25-15674S). The authors are also indebted to Dr V. Novohradský for performing experiments focused on the cellular localization of iridium complexes using a confocal microscope. Financial support from the Spanish Ministerio de Ciencia, Innovación y Universidades MICIU/AEI/10.13039/501100011033 and "ERDF A way of making Europe" through the projects PID2021-122850NB-I00 and PID2024-155371NB-I00 (J. R.) and CNS2024-154908 (A.

F.-M.) is acknowledged. A.F.-M. is grateful for the support of the Generalitat Valenciana (GV) through the project CIAICO/2022/121. M. E. A. acknowledges financial support under the PRIN D.D. 104/2022 PNRR M4.C2.1.1. – Project Code: 2022AN47CACUP: H53D23003820001, funded by the European Union NextGenerationEU – project title "La-G4-DACA" – Grant Assignment DD 862, 16/06/2023. M. E. A. is also grateful for the CINECA award under the ISCRA initiative, for access to high-performance computing resources and support (IsCc4_PAC-DACA project). I. R.-C. thanks Fundación Séneca for a predoctoral grant (project 21854/FPI/22). J. R. acknowledges support from Fundación Séneca-CARM (project 21989/PI/22). M. J. P.-M. acknowledges the financial support of MICIN/AEI/10.13039/501100011033 and the European Union (NextGenerationEU/PRTR) for her Juan de la Cierva Fellowship (IJC2020-045287-I).

References

1 M. Liu, Y. Chen, Y. Guo, H. Yuan, T. Cui, S. Yao, S. Jin, H. Fan, C. Wang, R. Xie, W. He and Z. Guo, Golgi apparatus-targeted aggregation-induced emission luminogens for effective cancer photodynamic therapy, *Nat. Commun.*, 2022, **13**, 2179.

2 J. Karges, Clinical development of metal complexes as photosensitizers for photodynamic therapy of cancer, *Angew. Chem., Int. Ed.*, 2022, **61**, e202112236.

3 X. Wang, J. Peng, C. Meng and F. Feng, Recent advances for enhanced photodynamic therapy: from new mechanisms to innovative strategies, *Chem. Sci.*, 2024, **15**, 12234–12257.

4 H. Shi, R. C. Marchi and P. J. Sadler, Advances in the design of photoactivatable metallodrugs: Excited state metallomics, *Angew. Chem., Int. Ed.*, 2025, **64**, e202423335.

5 Z. Deng, H. Li, S. Chen, N. Wang, G. Liu, D. Liu, W. Ou, F. Xu, X. Wang, D. Lei, P.-C. Lo, Y. Y. Li, J. Lu, M. Yang, M.-L. He and G. Zhu, Near-infrared-activated anticancer platinum(IV) complexes directly photooxidize biomolecules in an oxygen-independent manner, *Nat. Chem.*, 2023, **15**, 930–939.

6 H. Wang, Y. Lai, D. Li, J. Karges, P. Zhang and H. Huang, Self-assembly of erlotinib-platinum(II) complexes for epidermal growth factor receptor-targeted photodynamic therapy, *J. Med. Chem.*, 2024, **67**, 1336–1346.

7 N. Xu, G.-D. Zhang, Z.-Y. Xue, M.-M. Wang, Y. Su, H. Fang, Z.-H. Yu, H.-K. Liu, H. Lu and Z. Su, NIR photoactivated electron intersystem crossing to evoke calcium-mediated lysosome-dependent cell death and immunotherapy, *Chem. Eng. J.*, 2024, **497**, 155022.

8 Z. Xie, B. Cao, J. Zhao, M. Liu, Y. Lao, H. Luo, Z. Zhong, X. Xiong, W. Wei and T. Zou, Ion pairing enables targeted prodrug activation via red light photocatalysis: A proof-of-concept study with anticancer gold complexes, *J. Am. Chem. Soc.*, 2024, **146**, 8547–8556.

9 F. Chen, H. Ma, G. Wen, X. Wu, X. Lin, D. Li, D. Wang, A. Dao, H. Huang and P. Zhang, Regioisomerization strategy in iridium(III) complexes achieving enhanced type I photosensitization and tumor photoimmunotherapy, *J. Med. Chem.*, 2025, **68**, 13019–13029.

10 X.-Q. Zhou, P. Wang, V. Ramu, L. Zhang, S. Jiang, X. Li, S. Abyar, P. Papadopoulou, Y. Shao, L. Bretin, M. A. Siegler, F. Buda, A. Kros, J. Fan, X. Peng, W. Sun and S. Bonnet, In vivo metallophilic self-assembly of a light-activated anticancer drug, *Nat. Chem.*, 2023, **15**, 980–987.

11 L. M. Lifshits, J. A. Roque III, P. Konda, S. Monro, H. D. Cole, D. von Dohlen, S. Kim, G. Deep, R. P. Thummel, C. G. Cameron, S. Gujar and S. A. McFarland, Near-infrared absorbing Ru(II) complexes act as immunoprotective photodynamic therapy (PDT) agents against aggressive melanoma, *Chem. Sci.*, 2020, **11**, 11740–11762.

12 R. Bevernaegie, B. Doix, E. Bastien, A. Diman, A. Decottignies, O. Feron and B. Elias, Exploring the phototoxicity of hypoxic active iridium(III)-based sensitizers in 3D tumor spheroids, *J. Am. Chem. Soc.*, 2019, **141**, 18486–18491.

13 C. Imberti, P. Zhang, H. Huang and P. J. Sadler, New designs for phototherapeutic transition metal complexes, *Angew. Chem., Int. Ed.*, 2020, **59**, 61–73.

14 Y. Zhang, B.-T. Doan and G. Gasser, Metal-based photosensitizers as inducers of regulated cell death mechanisms, *Chem. Rev.*, 2023, **123**, 10135–10155.

15 Y. Wu, S. Li, Y. Chen, W. He and Z. Guo, Recent advances in noble metal complex based photodynamic therapy, *Chem. Sci.*, 2022, **13**, 5085–5106.

16 E. Ortega-Forte, A. Rovira, P. Ashoo, E. Izquierdo-García, C. Hally, D. Abad-Montero, M. Jordà-Redondo, G. Vigueras, A. Deyà, J. L. Hernández, J. Galino, M. Bosch, M. E. Alberto, A. Francés-Monerris, S. Nonell, J. Ruiz and V. Marchán, Achieving red-light anticancer photodynamic therapy under hypoxia using Ir(iii)–COUPY conjugates, *Inorg. Chem. Front.*, 2025, **12**, 3367–3383.

17 J. J. Ahrens, M. Denison, S. Garcia, S. Gupta, T. A. Kocarek, I. F. Sevrioukova, C. Turro and J. J. Kodanko, Mixed Ru(II)–Ir(III) complexes as photoactive inhibitors of the major human drug metabolizing enzyme CYP3A4, *Inorg. Chem.*, 2024, **63**, 18509–18518.

18 L. Holden, R. C. Curley, G. Avella, C. Long and T. E. Keyes, Targeting mitochondrial guanine quadruplexes for photoactivatable chemotherapy in hypoxic environments, *Angew. Chem., Int. Ed.*, 2024, **63**, e202408581.

19 A. Fennes, N. Montesdeoca, Z. Papadopoulos and J. Karges, Rational design of a red-light absorbing ruthenium polypyridine complex as a photosensitizer for photodynamic therapy, *Chem. Commun.*, 2024, **60**, 10724–10727.

20 R. J. Mitchell, D. Havrylyuk, A. C. Hachey, D. K. Heidary and E. C. Glazer, Photodynamic therapy photosensitizers and photoactivated chemotherapeutics exhibit distinct bioenergetic profiles to impact ATP metabolism, *Chem. Sci.*, 2025, **16**, 721–734.

21 H. D. Cole, J. A. Roque 3rd, G. Shi, L. M. Lifshits, E. Ramasamy, P. C. Barrett, R. O. Hodges, C. G. Cameron

and S. A. McFarland, Anticancer agent with iInexplicable potency in extreme hypoxia: Characterizing a light-triggered ruthenium ubertoxin, *J. Am. Chem. Soc.*, 2022, **144**, 9543–9547.

22 S. Monro, K. L. Colón, H. Yin, J. Roque, P. Konda, S. Gujar, R. P. Thummel, L. Lilge, C. G. Cameron and S. A. McFarland, Transition metal complexes and photodynamic therapy from a tumor-centered approach: Challenges, opportunities, and highlights from the development of TLD1433, *Chem. Rev.*, 2019, **119**, 797–828.

23 B. Kar, U. Das, N. Roy and P. Paira, Recent advances on organelle specific Ru(II)/Ir(III)/Re(I) based complexes for photodynamic therapy, *Coord. Chem. Rev.*, 2023, **474**, 214860.

24 L. C.-C. Lee and K. K.-W. Lo, Luminescent and photofunctional transition metal complexes: From molecular design to diagnostic and therapeutic applications, *J. Am. Chem. Soc.*, 2022, **144**, 14420–14440.

25 A. Zamora, G. Vigueras, V. Rodriguez, M. D. Santana and J. Ruiz, Cyclometalated iridium(III) luminescent complexes in therapy and phototherapy, *Coord. Chem. Rev.*, 2018, **360**, 34–76.

26 T. Kench, A. Rahardjo, G. G. Terrones, A. Bellamkonda, T. E. Maher, M. Storch, H. J. Kulik and R. Vilar, A semi-automated, high-throughput approach for the synthesis and identification of highly photo-cytotoxic iridium complexes, *Angew. Chem., Int. Ed.*, 2024, **63**, e202401808.

27 S. F. Kainat, M. B. Hawsawi, E. U. Mughal, N. Naeem, A. M. Almohyawi, H. M. Altass, E. M. Hussein, A. Sadiq, Z. Moussa, A. S. Abd-El-Aziz and S. A. Ahmed, Recent developments in the synthesis and applications of terpyridine-based metal complexes: a systematic review, *RSC Adv.*, 2024, **14**, 21464–21537.

28 B. Liu, S. Monro, Z. Li, M. A. Jabed, D. Ramirez, C. G. Cameron, K. Colón, J. Roque III, S. Kilina, J. Tian, S. A. McFarland and W. Sun, New class of homoleptic and heteroleptic bis(terpyridine) iridium(III) complexes with strong photodynamic therapy effects, *ACS Appl. Bio Mater.*, 2019, **2**, 2964–2977.

29 A. Chiarugi, C. Dölle, R. Felici and M. Ziegler, The NAD metabolome—a key determinant of cancer cell biology, *Nat. Rev. Cancer*, 2012, **12**, 741–752.

30 A. J. Covarrubias, R. Perrone, A. Grozio and E. Verdin, NAD+ metabolism and its roles in cellular processes during ageing, *Nat. Rev. Mol. Cell Biol.*, 2021, **22**, 119–141.

31 A. K. Yadav, R. Kushwaha, A. A. Mandal, A. Mandal and S. Banerjee, Intracellular photocatalytic NADH/NAD(P)H oxidation for cancer drug development, *J. Am. Chem. Soc.*, 2025, **147**, 7161–7181.

32 H. Huang, S. Banerjee, K. Qiu, P. Zhang, O. Blacque, T. Malcomson, M. J. Paterson, G. J. Clarkson, M. Staniforth, V. G. Stavros, G. Gasser, H. Chao and P. J. Sadler, Targeted photoredox catalysis in cancer cells, *Nat. Chem.*, 2019, **11**, 1041–1048.

33 Z. Fan, Y. Rong, T. Sadhukhan, S. Liang, W. Li, Z. Yuan, Z. Zhu, S. Guo, S. Ji, J. Wang, R. Kushwaha, S. Banerjee, K. Raghavachari and H. Huang, Single-cell quantification of a highly biocompatible dinuclear iridium(III) complex for photocatalytic cancer therapy, *Angew. Chem., Int. Ed.*, 2022, **61**, e202202098.

34 Q. Lie, H. Jiang, X. Lu, Z. Chen, J. Liang, Y. Zhang and H. Chao, Photo-activated ferrocene-iridium(III) prodrug induces immunogenic cell death in melanoma stem cells, *J. Med. Chem.*, 2025, **68**, 8894–8906.

35 V. Novohradsky, A. Marco, M. Svitelova, N. Cutillas, J. Ruiz and V. Brabec, Photoactivatable cyclometalated Ir(III) compound penetrates the blood-brain barrier in 3D spheroidal and advanced 3D organoid models of inherently resistant and aggressive brain tumors, *ACS Pharmacol. Transl. Sci.*, 2025, **8**, 2033–2047.

36 S. Chen, Z. Zhang, L. Wei, Z. Fan, Y. Li, X. Wang, T. Feng and H. Huang, Photo-catalytic Staphylococcus aureus inactivation and biofilm destruction with novel bis-tridentate iridium(III) photocatalyst, *Chin. Chem. Lett.*, 2023, **34**, 108412.

37 I. Singh, A. Upadhyay, A. A. Mandal, S. Saha, P. Pragya, L. Pradhan, M. Nayak, A. Dutta, A. K. Agrawal, S. Mukherjee and S. Banerjee, Fe(II)-photoantibiotics for potential antibacterial, antibiofilm, and infective wound healing applications in rat model, *J. Med. Chem.*, 2025, **68**, 4453–4465.

38 A. Yadav, S. S. Dindorkar and V. Patel, Untangling the effect of π-conjugation length on the opto-electronic properties of reactive dye-based sensitizer, *J. Comput. Electron.*, 2023, **22**, 1706–1714.

39 V. Nayana and B. Kandasubramanian, Polycarbazole and its derivatives: progress, synthesis, and applications, *J. Polym. Res.*, 2020, **27**, 285.

40 D. Annas, S.-Y. Cheon, M. Yusuf, S.-J. Bae, K.-T. Ha and K. H. Park, Synthesis and initial screening of lactate dehydrogenase inhibitor activity of 1,3-benzodioxole derivatives, *Sci. Rep.*, 2020, **10**, 19889.

41 L. Wei, A. Dao, G. Yuan, P. Zhang and H. Huang, In-cell NAD(P)H photocatalysis with a metal complex for photocatalytic anticancer therapy, *Acc. Chem. Res.*, 2025, **58**, 2640–2651.

42 J. Wang and G. S. Hanan, A facile route to sterically hindered and non-hindered 4′-aryl-2,2′:6′,2″-terpyridines, *Synlett*, 2005, 1251–1254.

43 V. Novohradsky, A. Marco, L. Markova, N. Cutillas, J. Ruiz and V. Brabec, Ir(III) compounds containing a terdentate ligand are potent inhibitors of proliferation and effective antimetastatic agents in aggressive triple-negative breast cancer cells, *J. Med. Chem.*, 2023, **66**, 9766–9783.

44 J. A. Porras, I. N. Mills, W. J. Transue and S. Bernhard, Highly fuorinated Ir(III)–2,2′:6′,2″-terpyridine–phenylpyridine–X complexes via selective C–F activation: Robust photocatalysts for solar fuel generation and photoredox catalysis, *J. Am. Chem. Soc.*, 2016, **138**, 9460–9472.

45 X. Wei, M.-J. Zhu, Z. Cheng, M. Lee, H. Yan, C. Lu and J.-J. Xu, Aggregation-induced electrochemiluminescence of carboranyl carbazoles in aqueous media, *Angew. Chem., Int. Ed.*, 2019, **58**, 3162–3166.

46 M. J. Frisch, G. W. Trucks, H. B. Schlegel, G. E. Scuseria, M. A. Robb, J. R. Cheeseman, G. Scalmani, V. Barone, G. A. Petersson, H. Nakatsuji, X. Li, M. Caricato, A. V. Marenich, J. Bloino, B. G. Janesko, R. Gomperts, B. Mennucci, H. P. Hratchian, J. V. Ortiz, A. F. Izmaylov, J. L. Sonnenberg, D. Williams-Young, F. Ding, F. Lipparini, F. Egidi, J. Goings, B. Peng, A. Petrone, T. Henderson, D. Ranasinghe, V. G. Zakrzewski, J. Gao, N. Rega, G. Zheng, W. Liang, M. Hada, M. Ehara, K. Toyota, R. Fukuda, J. Hasegawa, M. Ishida, T. Nakajima, Y. Honda, O. Kitao, H. Nakai, T. Vreven, K. Throssell, J. A. Montgomery Jr., J. E. Peralta, F. Ogliaro, M. J. Bearpark, J. J. Heyd, E. N. Brothers, K. N. Kudin, V. N. Staroverov, T. A. Keith, R. Kobayashi, J. Normand, K. Raghavachari, A. P. Rendell, J. C. Burant, S. S. Iyengar, J. Tomasi, M. Cossi, J. M. Millam, M. Klene, C. Adamo, R. Cammi, J. W. Ochterski, R. L. Martin, K. Morokuma, O. Farkas, J. B. Foresman and D. J. Fox, *Gaussian 16 Rev. A.03*, 2016.

47 M. Zgarbová, J. Šponer and P. Jurečka, Z-DNA as a touchstone for additive empirical force fields and a refinement of the alpha/gamma DNA torsions for AMBER, *J. Chem. Theory Comput.*, 2021, **17**, 6292–6301.

48 C. Adamo and V. Barone, Toward reliable density functional methods without adjustable parameters: The PBE0 model, *J. Chem. Phys.*, 1999, **110**, 6158–6170.

49 D. Andrae, U. Häußermann, M. Dolg, H. Stoll and H. Preuß, Energy-adjustedab initio pseudopotentials for the second and third row transition elements, *Theor. Chim. Acta*, 1990, **77**, 123–141.

50 Y. Zhao and D. G. Truhlar, The M06 suite of density functionals for main group thermochemistry, thermochemical kinetics, noncovalent interactions, excited states, and transition elements: two new functionals and systematic testing of four M06-class functionals and 12 other functionals, *Theor. Chem. Acc.*, 2008, **120**, 215–241.

51 R. L. Martin, Natural transition orbitals, *J. Chem. Phys.*, 2003, **118**, 4775–4777.

52 T. Holtum, J. Bloino, C. Pappas, V. Kumar, V. Barone and S. Schlücker, Ultraviolet resonance Raman spectroscopy of anthracene: Experiment and theory, *J. Raman Spectrosc.*, 2021, **52**, 2292–2300.

53 K. R. Naqvi and T. B. Melø, Reduction of tetranitromethane by electronically excited aromatics in acetonitrile: Spectra and molar absorption coefficients of radical cations of anthracene, phenanthrene and pyrene, *Chem. Phys. Lett.*, 2006, **428**, 83–87.

54 A. Manian and S. P. Russo, The dominant nature of Herzberg–Teller terms in the photophysical description of naphthalene compared to anthracene and tetracene, *Sci. Rep.*, 2022, **12**, 21481.

55 M. Baba, M. Saitoh, K. Taguma, K. Shinohara, K. Yoshida, Y. Semba, S. Kasahara, N. Nakayama, H. Goto, T. Ishimoto and U. Nagashima, Structure and excited-state dynamics of anthracene: Ultrahigh-resolution spectroscopy and theoretical calculation, *J. Chem. Phys.*, 2009, **130**, 134315.

56 C.-T. Wang, J. Chen, J. Xu, F. Wei, C. Y. Yam, K. M.-C. Wong, P. H. L. Sit and W. Y. Teoh, Selective visible light reduction of carbon dioxide over iridium(III)-terpyridine photocatalysts, *Mater. Today Chem.*, 2021, **22**, 100563.

57 J. Kasparkova, A. Hernández-García, H. Kostrhunova, M. Goicuría, V. Novohradsky, D. Bautista, L. Markova, M. D. Santana, V. Brabec and J. Ruiz, Novel 2-(5-arylthiophen-2-yl)-benzoazole cyclometalated iridium(III) dppz complexes exhibit selective phototoxicity in cancer cells by lysosomal damage and oncosis, *J. Med. Chem.*, 2024, **67**, 691–708.

58 A. Linero-Artiaga, L.-M. Servos, V. Rodríguez, J. Ruiz and J. Karges, Rationally designed Ir(III) complex with an exceptionally strong binding to human serum albumin for targeted photodynamic therapy, *J. Med. Chem.*, 2025, **68**, 7792–7806.

59 M. Redrado, E. Romanos, A. Benedi, G. Canudo-Barreras, I. Marzo, M. C. Gimeno and V. Fernández-Moreira, Synthetic ease and exceptional in vivo performance of pyrazole-based cyclometallated iridium complexes, *Inorg. Chem. Front.*, 2024, **11**, 1828–1838.

60 K. Choroba, J. Palion-Gazda, M. Penkala, P. Rawicka and B. Machura, Tunability of triplet excited states and photophysical behaviour of bis-cyclometalated iridium(III) complexes with imidazo[4,5-f][1,10]phenanthroline, *Dalton Trans.*, 2024, **53**, 17934–17947.

61 Y.-F. Kang, W.-K. Chen, K.-X. Teng, L.-Y. Wang, X.-C. Xu, L.-Y. Niu, G. Cui and Q.-Z. Yang, Aggregation turns BODIPY fluorophores into photosensitizers: Reversibly switching intersystem crossing on and off for smart photodynamic therapy, *CCS Chem.*, 2022, **4**, 3516–3528.

62 S.-Y. Yang, Y. Chen, R. T. K. Kwok, J. W. Y. Lam and B. Z. Tang, Platinum complexes with aggregation-induced emission, *Chem. Soc. Rev.*, 2024, **53**, 5366–5393.

63 G. Vigueras, E. Izquierdo-García, E. de la Torre-Rubio, D. Abad-Montero, M. D. Santana, V. Marchán and J. Ruiz, Metal–coumarin derivatives as promising photosensitizers: unlocking their cancer phototherapy potential, *Inorg. Chem. Front.*, 2025, **12**, 4355–4375.

64 Y. Yang, Y. Gao, J. Zhao and S. Gou, An electron-accepting half-sandwich iridium(III) complex for the treatment of hypoxic tumors via synergetic chemo- and phototherapy, *Inorg. Chem. Front.*, 2024, **11**, 436–450.

65 D. A. Case, H. M. Aktulga, K. Belfon, I. Y. Ben-Shalom, J. T. Berryman, S. R. Brozell, D. S. Cerutti, T. E. I. Cheatham, G. A. Cisneros, V. W. D. Cruzeiro, T. A. Darden, R. E. Duke, G. Giambasu, M. K. Gilson, H. Gohlke, A. W. Goetz, R. Harris, S. Izadi, S. A. Izmailov, K. Kasavajhala, M. C. Kaymak, E. King, A. Kovalenko, T. Kurtzman, T. S. Lee, S. LeGrand, P. Li, C. Lin, J. Liu, T. Luchko, R. Luo, M. Machado, V. Man, M. Manathunga, K. M. Merz, Y. Miao, O. Mikhailovskii, G. Monard, H. Nguyen, K. A. Hearn, A. Onufriev, F. Pan, S. Pantano, R. Qi, A. Rahnamoun, D. R. Roe, A. Roitberg, C. Sagui, S. Schott-Verdugo, A. Shajan, J. Shen, C. L. Simmerling, N. R. Skrynnikov, J. Smith, J. Swails, R. C. Walker, J. Wang,

J. Wang, W. H. Wei, R. M. Wolf, X. Wu, Y. Xiong, Y. Xue, D. M. York, S. Zhao and P. A. Kollman, *Amber 2022*, 2022.

66 I. S. Ufimtsev and T. J. Martínez, Quantum chemistry on graphical processing units. 1. Strategies for two-electron integral evaluation, *J. Chem. Theory Comput.*, 2008, **4**, 222–231.

67 I. S. Ufimtsev and T. J. Martinez, Quantum chemistry on graphical processing units. 2. Direct self-consistent-field implementation, *J. Chem. Theory Comput.*, 2009, **5**, 1004–1015.

68 I. S. Ufimtsev and T. J. Martinez, Quantum chemistry on graphical processing units. 3. Analytical energy gradients, geometry optimization, and first principles molecular dynamics, *J. Chem. Theory Comput.*, 2009, **5**, 2619–2628.

69 T. Yanai, D. P. Tew and N. C. Handy, A new hybrid exchange–correlation functional using the Coulomb-attenuating method (CAM-B3LYP), *Chem. Phys. Lett.*, 2004, **393**, 51–57.

70 A. M. A. Abdelgawwad and A. Francés-Monerris, easyPARM: Automated, versatile, and reliable force field parameters for metal-containing molecules with unique labeling of coordinating atoms, *J. Chem. Theory Comput.*, 2025, **21**, 1817–1830.

71 R. C. Walker, M. M. de Souza, I. P. Mercer, I. R. Gould and D. R. Klug, Large and fast relaxations inside a protein: Calculation and measurement of reorganization energies in alcohol dehydrogenase, *J. Phys. Chem. B*, 2002, **106**, 11658–11665.

72 J. J. Pavelites, J. Gao, P. A. Bash and A. D. Mackerell Jr., A molecular mechanics force field for NAD+ NADH, and the pyrophosphate groups of nucleotides, *J. Comput. Chem.*, 1997, **18**, 221–239.

73 H. Zhang, L. Tian, R. Xiao, Y. Zhou, Y. Zhang, J. Hao, Y. Liu and J. Wang, Anticancer effect evaluation in vitro and in vivo of iridium(III) polypyridyl complexes targeting DNA and mitochondria, *Bioorg. Chem.*, 2021, **115**, 105290.

74 J. Kasparkova, V. Novohradsky, J. Ruiz and V. Brabec, Photoactivatable, mitochondria targeting dppz iridium(III) complex selectively interacts and damages mitochondrial DNA in cancer cells, *Chem.-Biol. Interact.*, 2024, **392**, 110921.

75 J. Guo, W.-t. Yang, F.-y. Mai, J.-r. Liang, J. Luo, M.-c. Zhou, D.-d. Yu, Y.-l. Wang and C.-g. Li, Unravelling oncosis: morphological and molecular insights into a unique cell death pathway, *Front. Immunol.*, 2024, **15**, 1450998.

76 S. Zhou, R. Yamada and K. Sakamoto, Low energy multiple blue light-emitting diode light Irradiation promotes melanin synthesis and induces DNA damage in B16F10 melanoma cells, *PLoS One*, 2023, **18**, e0281062.

77 J. Zhuang, L. Xia, Z. Zou and J. Yin, Blue light induces ROS mediated apoptosis and degradation of AML1-ETO oncoprotein in Kasumi-1 cells, *Med. Oncol.*, 2022, **39**, 52.

78 V. Novohradsky, G. Vigueras, J. Pracharova, N. Cutillas, C. Janiak, H. Kostrhunova, V. Brabec, J. Ruiz and J. Kasparkova, Molecular superoxide radical photogeneration in cancer cells by dipyridophenazine iridium(III) complexes, *Inorg. Chem. Front.*, 2019, **6**, 2500–2513.

79 A. K. Yadav, V. Singh, I. Singh, A. Kunwar, B. Koch and S. Banerjee, Photocatalytic Anticancer Activity of Cyclometalated Ir(III) Complexes: A Mechanistic Insight, *Chem. – Asian J.*, 2025, **20**, e00681.

80 S. D. Varma, P. S. Devamanoharan and A. H. Ali, Prevention of Intracellular Oxidative Stress to Lens by Pyruvate and Its Ester, *Free Radical Res.*, 1998, **28**, 131–135.

81 D. C. Liemburg-Apers, P. H. Willems, W. J. Koopman and S. Grefte, Interactions between mitochondrial reactive oxygen species and cellular glucose metabolism, *Arch. Toxicol.*, 2015, **89**, 1209–1226.

82 B. Ghesquiere, B. W. Wong, A. Kuchnio and P. Carmeliet, Metabolism of stromal and immune cells in health and disease, *Nature*, 2014, **511**, 167–176.

83 C. Zhang, S. Cao, B. P. Toole and Y. Xu, Cancer may be a pathway to cell survival under persistent hypoxia and elevated ROS: A model for solid-cancer initiation and early development, *Int. J. Cancer*, 2015, **136**, 2001–2011.

84 CCDC 2497678: Experimental Crystal Structure Determination, 2025, DOI: **10.5517/ccdc.csd.cc2pv18w**.